NASA Contractor Report 4533

Large-Eddy Simulation of Laminar-Turbulent Breakdown at High Speeds With Dynamic Subgrid-Scale Modeling

Nabil M. El-Hady
Analytical Services & Materials, Inc.
Hampton, Virginia

Prepared for
Langley Research Center
under Contract NAS1-19320

National Aeronautics and
Space Administration
Office of Management
Scientific and Technical
Information Program
1993

LARGE-EDDY SIMULATION OF LAMINAR-TURBULENT BREAKDOWN AT HIGH SPEEDS WITH DYNAMIC SUBGRID-SCALE MODELING

Nabil M. El-Hady

Analytical Services & Materials, Inc.
Hampton, VA 23666

ABSTRACT

The laminar-turbulent breakdown of a boundary-layer flow along a hollow cylinder at Mach 4.5 is investigated with large-eddy simulation. The subgrid scales are modeled dynamically, where the model coefficients are determined from the local resolved field. The behavior of the dynamic-model coefficients is investigated through both an a priori test with direct numerical simulation data for the same case and a complete large-eddy simulation. Both formulations proposed by Germano et al. and Lilly are used for the determination of unique coefficients for the dynamic model, and their results are compared and assessed. The behavior and the energy cascade of the subgrid-scale field structure are investigated at various stages of the transition process. The investigations are able to duplicate a high-speed transition phenomenon observed in experiments and explained only recently by the direct numerical simulations of Pruett and Zang, which is the appearance of "rope-like" waves. We also investigate the nonlinear evolution and breakdown of the laminar boundary layer and the structure of the flow field during the transition process.

1. INTRODUCTION

In high-speed boundary-layer flows, the physics, prediction, and control of the laminar-turbulent transition process are of increasing fundamental, as well as technological importance because of such national projects as the design of the High-Speed Civil Transport (HSCT) and the National Aero-Space Plane (NASP). In contrast to the vast progress that has been made in understanding the different mechanisms of laminar breakdown to turbulence in incompressible flows, progress has been much slower for compressible flows because of the inherent complexity of high-speed numerical and laboratory experiments.

The road to transition in high-speed flows may involve several stages. First, an initial stage of linear instability of small disturbances, called primary instability, is well described by the compressible stability equations. (See Mack [1].) Multiple eigenvalues of high-frequency, amplified, and damped modes (Mack modes) appear in the solution of these equations. The first of the Mack modes is called the second mode, which is the most unstable of all the modes as a two-dimensional (2-D) disturbance. The linear stage is followed by a second stage, where apparent nonlinearity is revealed by the amplification of three dimensionality and the high growth rate of these disturbances. At this stage, the disturbances are still weak and the nonlinear distortion to the mean flow can be negligible. Studies of secondary instability mechanisms in high-speed flows (see El-Hady [2,3], Masad and Nayfeh [4], Ng and Erlebacher [5], Ng and Zang [6], and Pruett et al. [7]) have indicated that the growth rate of these three-dimensional (3-D) disturbances is more gradual; it persists for a long distance downstream, unlike the explosive and fast growth that was observed in incompressible flows. This may lead, in high-speed flows, to transition regions that are quite lengthy. These investigations have concluded that the subharmonic secondary instability is the most likely path to natural transition in high-speed flows. Finally, a strong nonlinear stage takes place with high and intense fluctuations that lead to the inevitable fully turbulent regime.

Experimental studies at high speeds have been reviewed by Kendall [8]. These studies stressed the fact that the second mode is the dominant instability in the high-speed range and is

responsible for the production of persisting, well-ordered, "rope-like" waves seen in photographs (e.g., Fischer and Weinstein [9]). In their direct numerical simulation (DNS) calculations of a Mach 4.5 flow along a hollow cylinder at the beginning of the laminar breakdown stage, Pruett and Zang [10] were able to reproduce this rope-like structure. They numerically generated a schlieren photograph (like the laboratory experiment), which was derived from the wall-normal density gradient, and concluded that these flow structures are associated with the subharmonic secondary instability and arise from the 2-D projection of the staggered 3-D lambda vortices.

The linear stability and secondary instability theories are not capable of describing the flow structure in the final stage that leads to laminar breakdown and afterwards. The recent approach of parabolized stability equations (PSE) [11,12] also has limitations and can describe the flow structure until just after the onset of transition. The flow structure during transition can only be described with DNS calculations. However, the application of compressible DNS to the laminar-turbulent transition process is an exceedingly expensive task because of the wide range of length scales present in the later stages of transition; hence, more resolution is needed in this stage than for laminar or fully turbulent flow. Typical temporal DNS computations require many hundreds of supercomputer hours; typical spatial DNS computations require thousands of hours. Because of its high computational requirement, DNS is usually used to simulate a forced transition to focus on the later stages of the transition process.

With the increased interest in boundary-layer transition of high-speed flows, given the high cost of compressible DNS and the problems associated with high-speed laboratory experiments, other, less computationally intensive methods are needed for engineering purposes. A large number of ongoing efforts by different researchers are aimed at developing such less computationally intensive methods that will make a distinct technological contribution to expanding the state of the art in this field with large-eddy simulation (LES).

The LES technique has been successfully applied to the study of turbulent flows (e.g., see the review article by Rogallo and Moin [13]) and has become an important method of

simulation. In DNS, all flow scales are accurately resolved; in LES, only the large energy-carrying scales are accurately resolved. The influence of the discarded small or subgrid scales (SGS) must be modeled appropriately to simulate the energy cascade (i.e., the energy transfer between the large and small scales). A filtering process is usually used to separate the large- and small-scale motions, which results in the appearance of the SGS in the residual stress and heat flux terms.

In LES, a unified SGS model is usually used for different types of flows because the small-scale motion is more universal for all types of flows. Specifically, in turbulent flows, the small-scale motions tend to be more isotropic and homogeneous; hence, they can be represented by simpler models, in comparison with the currently used Reynolds-averaged turbulence models. On the other hand, the large-scale motion differs sharply from one flow to another; it is directly affected by the boundary conditions. The main contribution of the model is that it allows the transfer of the correct amount of energy from the large to the subgrid scales, or vice versa, near the wall.

A central issue in LES is the development of models for the small subgrid scales. Contrary to turbulent flows, the SGS model used for transitional flows is required to capture several stages: the primary, the secondary, and the fully nonlinear stages. The model is also required to accurately predict the transition onset, the transition region, and the fully turbulent stage. A review of transition-region modeling was recently given by Singer [14]. The application of LES to transitional flows dictates numerous modifications and extensions for the conventional SGS models that are used for turbulent flows. Although the Smagorinsky eddy-viscosity model [15] remains the fundamental subgrid model in LES for incompressible flows, several extensions to this model have been made. Moin and Kim [16] used a damping function to account for the near-wall effects. Piomelli and Zang [17] modified the Smagorinsky model by using a scale function to avoid the known excessive damping of the SGS motion. The study by Piomelli et al. [18] established the feasibility of using LES for transitional flows. They applied this technique to the incompressible flat-plate boundary layer with a modified

Smagorinsky eddy-viscosity model. The results compare quite well with the corresponding DNS calculations.

The LES of high-speed flows has recently received increasing interest. For compressible isotropic turbulence, Speziale et al. [19] and Erlebacher et al. [20] have developed a compressible analog of the linear combination SGS model of Bardina et al. [21] (called the SEZH model); Zang et al. [22] used this model and found good agreement with the DNS data for 3-D compressible turbulence. Comte et al. [23], Lesieur et al. [24], and Normand and Lesieur [25] have developed and used a structure-function SGS model that is based on the physical implementation of the concept of eddy viscosity. They have applied the structure-function model to compressible isotropic turbulence, as well as to compressible transition. Kral and Zang [26] have tested both the SEZH model and the structure-function SGS model for supersonic turbulent flow over a flat plate and have concluded that the later model gives better agreement with experiments.

In all previous studies, the ad hoc manner in which the model constants and the model modifications (to satisfy certain physical conditions) have been treated is not satisfactory, so that the question always remains: can we make LES as attractive as DNS by eliminating the need for ad hoc models? Recently, Germano [27] and Germano et al. [28] have answered this question by introducing a new SGS eddy-viscosity model (dynamic model) for incompressible flows that avoids the ad hoc treatment and utilizes the spectral information in the large-scale field to evaluate the small-scale stresses. They applied this model to both channel and boundary-layer flows. Moin et al. [29] have extended the dynamic model to compressible flows and scalar transport and have applied it to the LES of decaying isotropic turbulence. El-Hady et al. [30] have established the feasibility of using the dynamic SGS model in the LES of high-speed transitional flows.

In this paper, we study the nonlinear evolution and breakdown of the laminar boundary layer in high-speed flows, as well as the structure of the flow field during the transition process. This study is achieved by using a large-eddy temporal simulation, where the large flow

structures are computed and the small scales are modeled. The flow field under study is the transitional axial flow field on an axisymmetric body (a hollow cylinder) at a Mach number of 4.5 and at a Reynolds number of 10000, based on the boundary-layer displacement thickness. We also study some aspects of the dynamic modeling of the small-grid scales applied to this transitional boundary layer. We expect the interaction, or the energy exchange, between the large and the small scales to be quite different in compressible transitional boundary layers in comparison with previous applications to isotropic turbulence and incompressible transition. In the remainder of the paper, we introduce the governing equations, develop the SGS dynamic model, and present the numerical procedures for the LES. We then discuss the results of both the a priori test for the model and the LES for a transitional boundary layer at a Mach number of 4.5. Finally, we close with some concluding remarks.

2. PROBLEM FORMULATION

Governing Equations

The axisymmetric flow field along a cylinder of radius R_a^* is described by the compressible 3-D Navier-Stokes and energy equations written in the body-fitted coordinate system x, y, z, where x is the direction along the body, y is the normal to the body, and z is the azimuthal direction. Lengths, velocities, and time are made dimensionless with the boundary-layer displacement thickness δ^* as a reference length, the edge velocity u_e^*, and δ^*/u_e^*, respectively. The pressure is made dimensionless with $\rho_e^* u_e^{*2}$. The temperature, density, specific heats, viscosity, and thermal conductivity of air are made dimensionless with their corresponding edge values. The displacement thickness δ^* is defined for the axisymmetric boundary layer by the quadratic equation

$$\delta^*[1 + \frac{\delta^*}{2R_a^*}] = \int_0^\infty \frac{r^*}{R_a^*} [1 - \frac{\rho^* u^*}{\rho_e^* u_e^*}] \, dy^* \tag{1}$$

where r^* is the radial coordinate defined as $r^*(y) = R_a^* + y^*$. Equation (1) reduces to the

standard planar boundary-layer definition as $R_a^* \to \infty$. In terms of these dimensionless quantities, the governing equations in vectorial form read

$$\frac{\partial \rho}{\partial t} + \nabla.(\rho \mathbf{V}) = 0 \tag{2}$$

$$\frac{\partial(\rho \mathbf{V})}{\partial t} + \nabla.(\rho \mathbf{V}\mathbf{V}) + \Lambda = -\nabla p + \frac{1}{R}\nabla.\sigma + \chi \tag{3}$$

$$\frac{\partial p}{\partial t} + \mathbf{V}.\nabla p + \gamma p \nabla.\mathbf{V} = \frac{1}{M_e^2 \Gamma R}\nabla.(k \nabla\theta) + \frac{\gamma - 1}{R}\Phi \tag{4}$$

with the state equation for an ideal gas

$$\gamma M_e^2 p = \rho\theta \tag{5}$$

In the above equations, σ is the dimensionless viscous stress tensor, and Φ is the dimensionless dissipation function. They are defined as

$$\sigma = \mu[\nabla\mathbf{V} + (\nabla\mathbf{V})^T] + \lambda\,(\nabla.\mathbf{V})\,\mathbf{I} \tag{6}$$

$$\Phi = \sigma:\nabla\mathbf{V} \tag{7}$$

Also, in this coordinate system, the vector operators are defined as

$$\nabla.\mathbf{V} \equiv \frac{\partial u}{\partial x} + \frac{R_a}{r}\frac{\partial w}{\partial z} + \frac{\partial v}{\partial y} + \frac{v}{r} \tag{8}$$

$$\mathbf{V}.\nabla p \equiv u\frac{\partial p}{\partial x} + \frac{R_a}{r}w\frac{\partial p}{\partial z} + v\frac{\partial p}{\partial y} \tag{9}$$

and some extra terms Λ and χ appear in the momentum equation; these are defined as

$$\Lambda \equiv -\frac{\rho w}{r}(0\ ,\ v\ ,\ -w) \tag{10}$$

$$\chi \equiv -\frac{1}{rR}(0\ ,\ \sigma_{xy}\ ,\ \sigma_{zz}) \tag{11}$$

Here, γ is the ratio of specific heats ($\gamma = 1.4$); M_e is the edge Mach number; $R = \rho_e\, u_e\, \delta^*/\mu_e$ is the Reynolds number; $\Gamma = c_p \mu_e / k_e$ is the Prandtl number ($\Gamma = 0.72$); μ and λ are the first and second coefficients of viscosity, respectively; k is the thermal conductivity; $\mathbf{I}$ is a unit tensor; and $(\,)^T$ denotes a transpose. The Stokes hypothesis is assumed, and the viscosity and thermal

conductivity are related to the temperature through Sutherland's law.

Instead of solving equations (2) through (5) directly for the full range of scales, we limit the resolvable scale size by explicitly applying the spatial filter G to each term in the Navier-Stokes and energy equations. This filtering process will separate the resolvable field from the SGS field, which is accomplished by decomposing each field quantity F in the flow domain D as

$$F = \bar{F} + F'' \tag{12}$$

where the filtered quantity $\bar{F}$ is defined as

$$\bar{F}(\mathbf{x},t) = \int_D G(\mathbf{x} - \zeta, \Delta)\, F(\zeta,t)\, d\zeta \tag{13}$$

and F'' is the SGS part that accounts for those scales not resolved by the filter width Δ. We note here that the filtered quantity $\bar{F}$ in equation (12) or (13) is a spatially averaged, time-dependent resolved quantity, rather than a time-averaged or ensemble-averaged mean quantity as in the Reynolds-averaged Navier-Stokes equations. We keep Δ as a parameter in the integral (equation (13)) to clearly show that the structure of the large-scale field and, consequently, the structure of the SGS field will depend on the filter width. The smallest scale allowed by the filter and the SGS model, which is $O(\Delta)$, should be greater than the smallest scale resolved by the grid size, which is $O(h)$. This relationship will ensure that the computations are independent of the numerical algorithm used in the simulations. In these calculations, we choose the filter width $\Delta_i = 2\, h_i$, where h_i is the grid size in the ith direction.

We use a sharp Fourier cutoff filter in these calculations and apply it in the wave space; it is conveniently defined as

$$\hat{G}_i(k_i) = \begin{cases} 1 & \text{for } k_i \le K_{ci} \\ 0 & \text{otherwise} \end{cases} \tag{14}$$

where $\hat{G}_i$ is the Fourier coefficient of the filter function in the ith direction and K_{ci} is the cutoff wave number in the ith direction (related to the corresponding filter width Δ_i by $K_{ci} = \pi/\Delta_i$). For laminar-turbulent transition flow problems, a cutoff filter is more appropriate than other

commonly used filters (e.g., a Gaussian filter or a variable-width box filter). This filter ensures clear identification of the SGS with scales that have wave numbers larger than the cutoff wave number K_{ci}, rather than a mixed identity with both small and large scales, which is the case for other filters (see Piomelli et al. [31]).

To account for large density fluctuations in high-speed flows, the resolved velocity and temperature fields are written in terms of Favre-filtered quantities (Speziale et al. [19]), which are defined as

$$\tilde{F} = \overline{\rho F}/\bar{\rho} \tag{15}$$

Now F is decomposed to

$$F = \tilde{F} + F' \tag{16}$$

where F' is the SGS part of F, based on Favre filtering; consequently, the Favre-filtered governing equations used for the large-eddy simulation are

$$\frac{\partial \bar{\rho}}{\partial t} + \nabla.(\bar{\rho}\tilde{\mathbf{V}}) = 0 \tag{17}$$

$$\frac{\partial(\bar{\rho}\tilde{\mathbf{V}})}{\partial t} + \nabla.(\bar{\rho}\tilde{\mathbf{V}}\tilde{\mathbf{V}}) + \overline{\mathbf{\Lambda}} = -\nabla\bar{p} + \frac{1}{R}\nabla.\bar{\boldsymbol{\sigma}} - \nabla.\boldsymbol{\tau} + \overline{\boldsymbol{\chi}} \tag{18}$$

$$\frac{\partial \bar{p}}{\partial t} + \tilde{\mathbf{V}}.\nabla\bar{p} + \gamma\bar{p}\nabla.\tilde{\mathbf{V}} = (\gamma - 1)(\overline{\mathbf{V}.\nabla p} - \tilde{\mathbf{V}}.\nabla\bar{p}) + \frac{1}{M_e^2 \Gamma R}\nabla.(\overline{k\nabla\theta}) + \frac{\gamma - 1}{R}\overline{\mathbf{\Phi}} - \frac{1}{M_e^2}\nabla.\mathbf{q} \tag{19}$$

with the state equation

$$\gamma M_e^2 \bar{p} = \bar{\rho}\tilde{\theta} \tag{20}$$

In deriving equations (17) through (20), we have utilized the commutative property of the filtering process with space and time such that

$$\frac{\overline{\partial F}}{\partial t} = \frac{\partial \bar{F}}{\partial t}, \qquad \overline{\nabla.F} = \nabla.\bar{F} \tag{21}$$

Also, we have decomposed the stress tensor $\bar{\rho}\widetilde{\mathbf{V}\mathbf{V}}$ into its resolved ($\bar{\rho}\tilde{\mathbf{V}}\tilde{\mathbf{V}}$) and SGS components ($\boldsymbol{\tau}$) and the heat flux $\bar{\rho}\widetilde{\mathbf{V}\theta}$ into its resolved ($\bar{\rho}\tilde{\mathbf{V}}\tilde{\theta}$) and SGS components ($\mathbf{q}$). Also, in the filtering

process, the extra term $\bar{\Lambda}$ that results from the use of a body-fitted coordinate system will contribute to the SGS; it is now defined as

$$\bar{\Lambda} = -\frac{\bar{\rho}\tilde{w}}{r}(0, \tilde{v}, -\tilde{w}) - \frac{1}{r}(0, \tau_{zy}, \tau_{zz}) \tag{22}$$

Equations (17) through (20) are further simplified by assuming that $\bar{\boldsymbol{\sigma}} = \boldsymbol{\sigma}(\tilde{\mathbf{V}})$, $(\gamma - 1)(\overline{\mathbf{V}.\nabla p} - \tilde{\mathbf{V}}.\nabla\bar{p}) = 0$, $\overline{k\nabla\theta} = \bar{k}\nabla\tilde{\theta}$, $\bar{\Phi} = \Phi(\tilde{\mathbf{V}})$, and neglecting the contribution to the SGS by the viscous dissipation.

The SGS stress tensor $\boldsymbol{\tau}$ and the SGS heat flux vector $\mathbf{q}$ appear in the right-hand side of the momentum and energy equations, respectively; they must be modeled to close these equations. The SGS stress tensor $\boldsymbol{\tau}$ consists of the Leonard, cross, and Reynolds stresses, which are defined as

$$L_{kl} = \bar{\rho}\,(\widetilde{\tilde{u}_k \tilde{u}_l} - \tilde{u}_k \tilde{u}_l) \tag{23}$$

$$C_{kl} = \bar{\rho}\,(\widetilde{u_k{}'\tilde{u}_l} + \widetilde{\tilde{u}_k u_l{}'}) \tag{24}$$

$$R_{kl} = \bar{\rho}\,(\widetilde{u'_k u'_l}) \tag{25}$$

The SGS heat flux vector $\mathbf{q}$ consists of similar components, which are defined as

$$qL_k = \bar{\rho}\,(\widetilde{\tilde{u}_k\tilde{\theta}} - \tilde{u}_k\tilde{\theta}) \tag{26}$$

$$qC_k = \bar{\rho}\,(\widetilde{u'_k\tilde{\theta}} + \widetilde{\tilde{u}_k\theta'}) \tag{27}$$

$$qR_k = \bar{\rho}\,(\widetilde{u'_k\theta'}) \tag{28}$$

Supplemented with appropriate initial and boundary conditions, equations (17) through (20) are used to yield the resolved flow field for all later times.

Modeling the Small-Grid Scales

To model the SGS stress tensor $\boldsymbol{\tau}$ and the SGS heat flux vector $\mathbf{q}$, we use the approach given by Speziale et al. [19] and Erlebacher et al. [20], which is based on the eddy-viscosity Smagorinsky model [15] and an analogous eddy diffusivity model; these are modeled as

$$\tau_{kl} = \bar{\rho}\,(\widetilde{\tilde{u}_k \tilde{u}_l} - \tilde{\bar{u}}_k \tilde{\bar{u}}_l) - 2C_r \bar{\rho}\Delta^2 |\tilde{S}| \tilde{S}_{kl}' + \frac{2}{3} C_i \bar{\rho}\Delta^2 |\tilde{S}|^2 \delta_{kl} \tag{29}$$

$$q_k = \bar{\rho}\,(\widetilde{\tilde{u}_k \tilde{\theta}} - \tilde{\bar{u}}_k \tilde{\bar{\theta}}) - C_\theta \bar{\rho}\Delta^2 |\tilde{S}| \frac{\partial \tilde{\theta}}{\partial x_k} \tag{30}$$

where δ_{kl} is the Kronecker delta. The characteristic filter width Δ and the Favre-filtered rate-of-strain tensor $\tilde{S}_{kl}$ are defined as

$$\Delta = (\Delta_x\ \Delta_y\ \Delta_z)^{1/3} \tag{31}$$

$$\tilde{S}_{xx} = \frac{\partial \tilde{u}}{\partial x} \tag{32a}$$

$$\tilde{S}_{xz} = \frac{1}{2}\left(\frac{R_a}{r}\frac{\partial \tilde{u}}{\partial z} + \frac{\partial \tilde{w}}{\partial x}\right) \tag{32b}$$

$$\tilde{S}_{xy} = \frac{1}{2}\left(\frac{\partial \tilde{u}}{\partial y} + \frac{\partial \tilde{v}}{\partial x}\right) \tag{32c}$$

$$\tilde{S}_{zz} = \frac{R_a}{r}\frac{\partial \tilde{w}}{\partial z} + \frac{\tilde{v}}{r} \tag{32d}$$

$$\tilde{S}_{zy} = \frac{1}{2}\left(\frac{R_a}{r}\frac{\partial \tilde{v}}{\partial z} + \frac{\partial \tilde{w}}{\partial y} - \frac{\tilde{w}}{r}\right) \tag{32e}$$

$$\tilde{S}_{yy} = \frac{\partial \tilde{v}}{\partial y} \tag{32f}$$

and

$$\tilde{S}_{kl}' = \tilde{S}_{kl} - \frac{1}{3}\tilde{S}_{kk}\delta_{kl} \tag{33}$$

$$|\tilde{S}| = (2\,\tilde{S}_{kl}\tilde{S}_{kl})^{1/2} \tag{34}$$

Note that the first term in equations (29) and (30) represents the scale similarity part of the model; it is the sum of the Leonard and cross portions of the SGS stress or heat flux fields. The remaining part of the equation represents the model for the Reynolds portion of the stress or heat flux fields. Piomelli et al. [31] indicated the need for the model to be consistent with the type of filter used in the analysis. With the cutoff filter, the scale similarity portion of the model is neglected, and the SGS field is modeled by the eddy-viscosity and its analogous

eddy-diffusivity portions. The coefficients of the model C_r, C_i, and C_θ are to be determined.

The Dynamic Model

In accordance with Germano et al. [28] and Moin et al. [29], the filtered equations of motion (equations (17) through (20)) are filtered once more. Again, a sharp Fourier cutoff filter is applied in the wave space (see equation (14)), where $\hat{\Delta}_i$ represents the new filter width in the ith direction and the ratio $\delta = \hat{\Delta}_i/\Delta_i > 1$. A ratio of $\delta = 2$ is adopted in the present calculations. The filter is applied in the x-direction along the body and in the z-azimuthal direction; no filter is applied in the direction normal to the wall. The first and the second filters, usually called grid and test filters, respectively, will each produce a resolved flow field. The difference between the two resolved fields is the contribution by the small scales of length between the first and the second filter widths. In deriving a dynamic model, several assumptions are made, which we will identify. First, the same type of filter (a sharp Fourier cutoff filter) is used in both the grid and test filtering. Second, the same functional form, based on the Smagorinsky eddy-viscosity closure, is used to model the SGS stress terms from both filters. Third, the same functional form based on an analogous eddy-diffusivity closure is used to model the SGS heat flux terms from both filters. Fourth, a plane-averaging process is used in the derivation of the model coefficients, where the averaging is taken over a plane that is parallel to the wall. Finally, the model coefficients are independent of the filtering process. Each of these assumptions has its merits and can open the way for future adjustments of the dynamic model (e.g., Ronchi et al. [32] and Ghosal et al. [33]). Here, we briefly describe the derivation of the model and leave the details to other references. (See references [28] and [29]).

In accordance with Germano et al. [28] and Moin et al. [29], we apply a test filter to the equations of motion (17) through (20). We again use a sharp Fourier cutoff filter in the x-direction along the body and in the z-azimuthal direction (with no filtering in the y-direction that is normal to the wall). This new filter has the characteristic width

$$\hat{\Delta} = (\delta\Delta_x\ \Delta_y\ \delta\Delta_z)^{1/3} \tag{35}$$

The SGS stresses and heat flux that appear in equations (18) and (19) can be defined as

$$\tau_{kl} = \bar{\rho}\,(\widetilde{u_k u_l} - \tilde{u}_k \tilde{u}_l) \tag{36}$$

$$q_k = \bar{\rho}\,(\widetilde{u_k \theta} - \tilde{u}_k \tilde{\theta}) \tag{37}$$

Analogous to the above equations, the SGS stresses and heat flux that appear in the test-filtered equations can be defined as

$$T_{kl} = \hat{\bar{\rho}}\,(\widehat{\widetilde{u_k u_l}} - \hat{\tilde{u}}_k \hat{\tilde{u}}_l) \tag{38}$$

$$Q_k = \hat{\bar{\rho}}\,(\widehat{\widetilde{u_k \theta}} - \hat{\tilde{u}}_k \hat{\tilde{\theta}}) \tag{39}$$

By assuming the same functional form and model coefficients and neglecting the similarity portion, the "test" SGS stresses and heat flux are modeled the same way as in equations (29) and (30), with the scale similarity portion neglected as

$$T_{kl} = -2C_r \hat{\bar{\rho}} \hat{\Delta}^2 |\hat{\tilde{S}}| \hat{\tilde{S}}_{kl}' + \frac{2}{3} C_i \hat{\bar{\rho}} \hat{\Delta}^2 |\hat{\tilde{S}}|^2 \delta_{kl} \tag{40}$$

$$Q_k = - C_\theta \hat{\bar{\rho}} \hat{\Delta}^2 |\hat{\tilde{S}}| \frac{\partial \hat{\tilde{\theta}}}{\partial x_k} \tag{41}$$

The grid-filtered SGS field and the test-filtered SGS field are related by the Germano identity [27], such that

$$D_{kl} \equiv T_{kl} - \hat{\tau}_{kl} = \widehat{\bar{\rho} \tilde{u}_k \tilde{u}_l} - \hat{\bar{\rho}} \hat{\tilde{u}}_k \hat{\bar{\rho}} \hat{\tilde{u}}_l / \hat{\bar{\rho}} \tag{42}$$

$$E_k \equiv Q_k - \hat{q}_k = \widehat{\bar{\rho} \tilde{u}_k \tilde{\theta}} - \hat{\bar{\rho}} \hat{\tilde{u}}_k \hat{\bar{\rho}} \hat{\tilde{\theta}} / \hat{\bar{\rho}} \tag{43}$$

where D_{kl} and E_k are computable from the resolved large-eddy field. They are the resolved components of the stress tensor with scales of motion between the test and the grid scales. Lilly [34] called it the test window.

By using the traces of equations (29), (40), and (42), the following expression can be derived to solve for C_i

$$D_{kk} = 2C_i (\hat{\Delta}^2 \hat{\bar{\rho}} |\hat{\tilde{S}}|^2 - \Delta^2 \widehat{\bar{\rho} |\tilde{S}|^2}) = C_i B \tag{44}$$

By substituting equations (29), (40), and (44) into equation (42) and equations (30) and (41)

into equation (43), the following expressions can be derived to solve for C_r and C_θ:

$$D_{kl} - \frac{1}{3}D_{kk}\delta_{kl} = -2C_r(\hat{\Delta}^2\hat{\bar{\rho}}|\hat{\tilde{S}}|\hat{\tilde{S}}_{kl}' - \Delta^2\widehat{\bar{\rho}|\tilde{S}|\tilde{S}_{kl}'}) = C_r M_{kl} \tag{45}$$

$$E_k = -C_\theta(\hat{\Delta}^2\hat{\bar{\rho}}|\hat{\tilde{S}}|\frac{\partial\hat{\tilde{\theta}}}{\partial x_k} - \Delta^2\widehat{\bar{\rho}|\tilde{S}|\frac{\partial\tilde{\theta}}{\partial x_k}}) = C_\theta N_k \tag{46}$$

Each of the expressions (45) and (46) represents a set of six independent equations in one unknown. In order to uniquely determine the model coefficients C_r and C_θ, we use the contractions proposed by Germano et al. [28] and Moin et al. [29] in which equation (45) is contracted with $\tilde{S}_{kl}$ and equation (46) is contracted with $\partial\tilde{\theta}/\partial x_k$. We refer to this contraction as c_1 in our calculations. We also use another contraction obtained from the least-squares analysis of Lilly [34] in which equation (45) is contracted with M_{kl} and equation (46) is contracted with N_k. We refer to this contraction as c_2 in our calculations. The model coefficients in expressions (44), (45), and (46) are functions of space and time. They can locally become negative, which allows for backscatter (i.e., the transfer of energy from the SGS to the large scale). In their DNS calculations of transitional and turbulent channel flows, Piomelli et al. [35] have shown that about half of the grid points experience a backscatter when a Fourier cutoff filter is used. To alleviate an observed numerical instability caused by ill-conditioned local quantities, we perform a spatial averaging technique in a plane parallel to the wall (indicated by $< >$). This plane averaging enhances the numerical stability of the simulations at the expense of losing some of the conceptual advantages of the dynamic modeling formulation. The plane averaging leads to the following expressions for the model coefficients:

$$C_i = \frac{< D_{kk} >}{< B >} \tag{47}$$

$$C_r = \frac{< (D_{kl} - D_{kk}\delta_{kl}/3)\,\chi_{kl} >}{< M_{kl}\,\chi_{kl} >} \tag{48}$$

$$C_\theta = \frac{< E_k\Lambda_k >}{< N_k\Lambda_k >} \tag{49}$$

where χ_{kl} and Λ_k assume the value given by the type of contraction. With the calculation of

the model coefficients, equations (29) and (30) are used to calculate the SGS stresses and the heat flux to close the governing equations (17) through (20).

3. TESTING THE DYNAMIC MODEL

In this section, we investigate the behavior of the dynamic model coefficients using the DNS data of Pruett and Zang [10] for a transitional boundary-layer flow along a hollow cylinder at a Mach number of 4.5. This so called a priori test serves as a qualitative evaluation of the model coefficients, the modeled SGS stresses, and the heat flux at various stages of the laminar-turbulent transition process. It also serves as an assessment of the two types of contractions that are used in calculating a unique value for the coefficients of the dynamic model. But, one should note that the output of an a priori test may not include the anticipated interaction between the modeled scales and the large scales, which can only be achieved through a complete LES.

The initial resolution of the DNS data at time $t = 0$ was $12 \times 6 \times 96$ in the streamwise, azimuthal, and wall normal directions respectively (symmetry was enforced about the plane $z = 0$ to reduce the number of grid points by half in the azimuthal direction). As time evolved, the streamwise and azimuthal grid refinements were made as necessary to maintain at least a difference of eight orders of magnitude between the most and the least energetic Fourier harmonics. A well-resolved flow field was reached until the period 55 (time is given here in terms of the period of the primary wave) with a resolution of $96 \times 48 \times 144$, beyond which the simulation became increasingly ill-resolved.

We use the DNS data to examine the model coefficients on a coarse grid that is overlayed on top of the fine DNS grid. The effect of the filter width is investigated first by applying the grid filters $48 \times 24 \times 96$, $32 \times 16 \times 96$, and $24 \times 12 \times 96$ to the DNS data (which correspond to Fourier cutoff wave numbers of 24, 16, and 12, respectively, in the streamwise and azimuthal directions). To evaluate the dynamic model coefficients, test filters are then applied to the DNS data and the ratio $\delta = 2$ is kept fixed. All calculations in this paper enforce a symmetry

about the plane $z = 0$ to reduce by half the number of grid points in the azimuthal direction. The numerical grid is always given in this order: streamwise, symmetric azimuthal, and wall-normal directions.

We find that the model coefficients C_r, C_i, and C_θ have a zero value at the wall and vanish in the free stream; they oscillate at locations in the wall region. The coefficients are very small in the early linear region, and their values increase sharply as the laminar breakdown begins. Figure 1 shows the effect of the filter width on the plane-averaged values of the model coefficients at $t = 54$ inside the transition region. Their values increase as the filter width increases (coarser grid). A very coarse grid results in a sharp rise in the value of the coefficient with high oscillations in the wall region. This result will have a direct effect on the amount of energy contained in the SGS as the filter width changes. For example, Fig. 2 shows this effect on the plane-averaged values of the component τ_{xz} of the SGS Reynolds stress tensor, the SGS kinetic energy K, and the component q_z of the SGS heat flux vector. Contraction c_1 is used in the calculations of Figs. 1 and 2. Figure 2 shows that the SGS stress, heat flux, and energy are very small for the grid $48 \times 24 \times 96$ (as compared to the corresponding resolved quantities in Fig. 17 below), which indicates that with the Fourier cutoff filter the grid $48 \times 24 \times 96$ might be capable of resolving the flow field without modeling.

The ratio δ is the only input parameter needed for the dynamic model. For a fixed-grid filter, the effect of changing δ on the model coefficients is expected to be the same as changing the grid filter in Fig 1. As δ increases, the test-filter width increases which results in high oscillations in the model coefficients and, consequently, in the SGS field. Figures 3 and 4 show that effect on the model coefficients and the SGS field, respectively, at $t = 54$ using contraction c_2. The ratio $\delta = 3$ gives high oscillations in the wall-normal distribution of C_r, C_θ, and the SGS Reynolds stress and heat flux. A ratio of $\delta = 1.3$ results in negative values of C_i and the SGS turbulent kinetic energy. The ratio $\delta = 2$ is kept fixed throughout all the calculations.

An example of the effect of the proposed contractions c_1 and c_2 is shown in Figs. 5 and 6. Figure 5 illustrates the effect on the coefficients C_r and C_θ. Figure 6 shows the effect on the

component τ_{xz} of the SGS stress and on the component q_z of the SGS heat flux, which is given for a grid filter $32 \times 16 \times 96$ at $t = 54$. The effect is a typical example for other grid filters and for different times. The contraction c_2 obtained from the least-squares analysis produces model coefficients, as well as SGS stress and heat flux components, that are more than 50 percent less than their counterparts with the contraction c_1. Note that the model coefficient C_i and, therefore, the SGS kinetic energy are not affected by the type of contraction in an a priori test. We will show in section 5 that this may not be the case for a complete numerical simulation. Although the numerator and the denominator of the expressions in equations (47) through (49) are dealiased, the high oscillations persist, as shown in the figures for the model coefficients and the SGS field. These oscillations are probably unphysical and caused by ill-conditioned behavior.

4. NUMERICAL PROCEDURES FOR LARGE-EDDY SIMULATIONS

The solution of equations (17) through (20) uses basically the same algorithm used by Erlebacher and Hussaini [36] to simulate compressible flow over a flat plate, and by Pruett and Zang [10] to simulate compressible flow over axisymmetric bodies. Here, we briefly describe the main features of the algorithm.

Because the parallel mean flow does not satisfy the governing equations (17) through (20), forcing terms are added to the right-hand side of these equations to suppress the temporal evolution of the unperturbed mean flow, so that the laminar state becomes stationary. The initial value problem defined by equations (17) through (20) is explicitly integrated in time by using a third-order low-storage Runge-Kutta method. The time step is automatically controlled by the minimum of the maximum time steps allowed by the linearized advection and diffusion problems. The streamwise and the azimuthal directions are periodic so that the flow variables can be represented by Fourier series in these directions. The periodicity lengths in the streamwise and azimuthal directions ($2L_x$ and L_z) are related to the corresponding wave numbers α and β by $L_x = 2\pi/\alpha$ and $L_z = 2\pi/\beta$. The spatial derivatives in these directions are evaluated at

each time step by spectral collocation methods. In the wall-normal direction, a sixth-order compact difference scheme is implemented. To increase the resolution requirements in the direction normal to the wall without drastically decreasing the time step in an explicit scheme, Pruett and Zang [10] have implemented a sixth-order compact difference scheme in the wall-normal direction, instead of the Chebychev collocation method used by Erlebacher and Hussaini [36].

The grid is uniform in the x- and z-directions; a mapping is used in the y-direction, which clusters points near the wall and the critical layer and stretches the grid toward the far-field boundary. Symmetry is enforced about the plane $z = 0$ to save computational time. Spectral methods are known to introduce both truncation and aliasing errors. To minimize these errors, we adopted the same method as in Ref. [10]; we check the decay of the spectrum of the Fourier coefficients and refine the grid accordingly as needed.

Equations (47) through (49) are used to evaluate the model coefficients at each time step from the flow field at the previous time step. The SGS stresses and heat flux are evaluated with equations (29) and (30) at each time step and added to the right-hand side before the governing equations are advanced in time.

At each time step, the energy content $E_{\alpha\beta}$ in any Fourier mode (α,β), normalized with the mean-flow energy E_0 is calculated from the Fourier coefficients of the velocity $\hat{v}_{\alpha,\beta}$ as

$$E_{\alpha,\beta}(t) = \frac{d_\alpha d_\beta}{2E_0} \int_0^{y_{max}} \bar{\rho}(y) \, |\hat{v}_{\alpha,\beta}(y,t)|^2 \, \frac{r(y)}{R_a} dy$$

$$d_k = 2 - \delta_{k0} \tag{50}$$

Simulations are carried out for the flow along a cylinder with a Mach number of 4.5, a stream temperature of 110^0R at the edge of the boundary layer, and at a streamwise station that corresponds to $R = 10000$.

The initial conditions for the temporal numerical simulation match those of the DNS of reference [10]. They consist of the mean flow over a hollow cylinder $q_0(y)$, an axisymmetric

second-mode primary disturbance $q_1(x,y,t)$, and a secondary subharmonic disturbance $q_2(x,y,z,t)$. The mean flow is a spectral solution of the axisymmetric compressible boundary layer [37]. The solution of the primary disturbance [5] assumes the form

$$q_1(x,y,t) = \varepsilon_1 \, [\tilde{q}_1(y) \, e^{i(\alpha x - \omega t)} + cc] \tag{51}$$

and the solution of the secondary disturbance [7] assumes the form

$$q_2(x,y,z,t) = \varepsilon_2 \, [e^{i\alpha(x-\omega t/\alpha)/2} \, e^{i\beta R_a z} \sum_{n=-N}^{N} \tilde{q}_{2,n}(y) \, e^{in\alpha(x-\omega t/\alpha)} + cc] \tag{52}$$

where $\alpha = 0.2523$ and $\omega = 0.2285 + i\,0.319 \times 10^{-3}$ are, respectively, the real wave number and the complex frequency of a primary disturbance of amplitude $\varepsilon_1 = 0.085$. The secondary disturbance has four wave components ($N = 4$), an azimuthal wave number $\beta = 0.2673$, and an amplitude $\varepsilon_2 = 0.017$. The eigenfunctions of both the primary and secondary disturbances are normalized such that their amplitudes measure the maximum root-mean-square value of the corresponding temperature disturbance.

Dirichlet boundary conditions are applied to the total flow (except density) at the wall and at the far field. The density is calculated by projecting forward in time with the Runge-Kutta integrator, and the state equation is used to calculate the pressure.

5. RESULTS OF LARGE-EDDY SIMULATIONS

Features of the Dynamic Model

A large-eddy simulation is conducted with the dynamic model and the initial grid 24 × 12 × 96 by using the contraction c_2 and $\delta = 2$. The grid is fixed at 24 × 12 × 96 throughout the transition region. Figure 7 shows the time evolution of the dynamic model coefficients C_r, C_i, and C_θ. Although the coefficients are functions of y and t, they are averaged in the wall-normal direction for the purpose of this graph. The figure illustrates one of the favorable characteristics of the dynamic model; it turns itself off and on without the need for any added ad hoc functions. The model is turned off in the linear and weakly nonlinear regions. These

regions are approximated from the evolution of the primary and secondary disturbances; the linear region is between the period 0 and the period 15, and the weakly nonlinear region follows until the period 35. The model turns itself on in the strong nonlinear region (from periods 35 to 45). The value of the model coefficients gradually increases as the laminar breakdown commences, continues to increase through the transition region, and then decreases again in the fully turbulent region.

A second LES is conducted in which a grid of $24 \times 12 \times 96$ is used at the initial stages, and is refined as necessary to maintain at least a difference of four orders of magnitude between the most and the least energetic Fourier harmonics. The final grid reached is $48 \times 24 \times 96$. The time evolution of the dynamic model coefficients C_r, C_i, and C_θ (averaged in y) is included in Fig. 7 for comparison with the first LES of grid $24 \times 12 \times 96$.

For the LES with final grid $48 \times 24 \times 96$, we examine the evolution of the wall-normal distribution of the model coefficients with time. Figure 8 shows the y-variation of plane-averaged values of C_r, C_i, and C_θ at $t = 45$, $t = 54$, and $t = 62$, which correspond to nearly the beginning, the middle, and the end of the transition region. First, the figure shows that the model gives the proper asymptotic behavior near the wall and vanishes in the free stream (without the need for ad hoc damping functions). As y approaches the free stream, we notice in the calculations that either the numerator of the formula for the model coefficient goes to zero or both the numerator and the denominator go to zero. In the later case, we assign a zero value for the model coefficient. Second, the model is first turned off and then turned on automatically in the transition region (without the need for an ad hoc intermittency function). Third, the values of the model coefficients are almost negligible in the linear and early nonlinear stages and increase sharply in the wall region as the breakdown progresses. As the turbulent stage approaches, the values of the model coefficients drop and are not confined to the wall region, but spread away from the wall (not shown). At any plane parallel to the wall, the model coefficient $C_i(x,z,t)$ is always positive by the definition of the SGS kinetic energy, although negative values of C_i sometimes occur during the calculations (see Fig. 8) in the

linear and the early nonlinear stages when the SGS kinetic energy is very small. This result leads to speculation on the validity of using the dynamic model to accurately represent the physics of flow fields that are dominated by the large-scale structure. On the other hand, model coefficients $C_r(x,z,t)$ and $C_\theta(x,z,t)$ can take a positive or negative value, but their plane-averaged values are rarely negative.

The plane-averaged value of the turbulent Prandtl number Pr_t is defined by the ratio C_r/C_θ. This parameter directly influences the modeling of the SGS heat flux in Eq. (30). In the y-region, where both C_r and C_θ have a nonzero value, Fig. 9 shows the evolution of the wall-normal distribution of the turbulent Prandtl number with time. The figure indicates that Pr_t reaches an average value of 0.2 to 0.5 in the transition region.

Contraction c_1 is used in the simulations that produced Fig. 8. When contraction c_2 is used, similar observations are noted in addition to the reduction in the value of the model coefficients predicted by the a priori test. Figures 10 and 11 show the effect of the contraction type on the model coefficients at $t = 54$ and $t = 62$, respectively. Although the type of contraction does not affect the value of C_i in an a priori test, a large-eddy simulation does affect their values, most probably because of the interaction between the modeled and large scales. Although the values for C_r and C_θ predicted by the contraction c_1 are higher than those predicted by the contraction c_2, the value of C_i calculated with contraction c_1 is slightly lower than that calculated with contraction c_2 as shown in Figs. 10 and 11.

Global Features of the Flow Field

For the LES with a fixed grid at 24 × 12 × 96 throughout the transition region, we checked the one-dimensional energy spectra against the corresponding spectra of a coarse-grid DNS (no SGS model) and a fine-grid DNS. The coarse-grid DNS seems capable of resolving the flow field only to a stage near the onset of transition. Its one-dimensional energy spectra in both the streamwise and the spanwise directions gives good agreement with the fine-grid DNS until $t = 50$. Beyond $t = 50$ and inside the transition region, the disagreement is slightly

enhanced by the dynamic SGS model because of the large increase in the value of the model coefficients. However, the dynamic model with the 24 × 12 × 96 grid seems unable to provide the right amount of energy transfer between the large and subgrid scales, as shown in Fig. 12 at t = 55. Also, the energy content of some of the principal modes (Fourier harmonics) is checked against the corresponding energy content of a fine-grid DNS. This check demonstrates that the dynamic model with the grid 24 × 12 × 96 is capable of predicting the correct energy content of various Fourier modes only to a stage near the onset of transition.

For the second LES calculations, where we reached a final grid of 48 × 24 × 96, Fig. 13 shows the one-dimensional spectra of the kinetic energy in both the streamwise and spanwise directions at t = 55 (where the grid is 36 × 24 × 96). The figure exhibits good agreement with the fine-grid DNS.

Figure 14 shows the time evolution of the principal Fourier harmonics in terms of its energy content. Of these, three harmonics ((1,0), (1/2,1), and (3/2,1)) are present in the initial conditions (together with their complex conjugates); however, the others ((0,2), (1,2), and (2,2)) emerged from the self-interaction of different components of the secondary disturbance. The different stages of evolution (linear, weakly nonlinear, strongly nonlinear, and breakdown) are recognized in accordance with the development of the primary mode (1,0) and the secondary subharmonics (1/2,1) and (3/2,1). The evolution of the various modes agrees well with the fine-grid DNS [10]. Of interest is the LES prediction of the domination of the mode (0,2) near the period 30 as indicated by the DNS [10].

In Figs. 15 and 16, we show a close comparison inside the transition region between the two LES presented in this paper (with grids 24 × 12 × 96 and 48 × 24 × 96) and the fine-grid DNS 96 × 48 × 144 of Pruett and Zang [10] for the energy content of the principal modes (1,0), (1/2,1), (0,1), and (0,2). The dynamic model with the grid 48 × 24 × 96 shows good agreement with the DNS and is capable of predicting the correct energy content of various Fourier modes all the way to and through the transition region; as mentioned before, in the case of the dynamic model with the grid 24 × 12 × 96, the comparison stops near the onset of

transition.

The evolution of the model coefficients will directly influence the development of the SGS stresses and the SGS heat flux. However, the local values of the SGS field are not essential to the evolution of the large-scale field. The divergence of the SGS field is the quantity that enters the momentum and energy equations. Figure 17 shows the development of the resolved field with time. The figure gives the y-variation of the plane-averaged values of the Reynolds stress component τ_{xz}, the kinetic energy K, and the heat flux component q_z at progressive times. The figure also shows a comparison with the fine-grid DNS results at $t = 45$ and $t = 54$, where the DNS results are filtered on the same grid that is used for the LES. Fine-grid DNS results are not available at $t = 62$.

Figure 18 shows the effect of the contraction type on the resolved field and a comparison with the fine-grid DNS results at $t = 54$. The fine-grid DNS results are filtered on the same grid that is used for the LES. Although both types of contraction resulted in a resolved field that is slightly overpredicted at this time ($t = 54$), contraction c_2 is better able to predict the peak values than contraction c_1.

The time evolution of the shape factor H and the plane-averaged skin friction C_f are shown in Fig. 19. The results from both types of contraction are compared with a fine-grid DNS and a coarse-grid DNS. The coarse-grid DNS is the same grid used for LES, but without the SGS modeling. A remarkable agreement exists between LES calculations and the fine DNS results, which indicates that the dynamic model ensures the transfer of the correct amount of energy between the large and the subgrid scales. Without the SGS dynamic modeling, the coarse-grid DNS results fail to predict the evolution of the skin friction during the transition region. Notice that both types of contraction used in the LES calculations give the same results until the end of the transition region, where some differences appear.

The Structure of the Flow Field

The subharmonic secondary instability is the most likely path to natural transition in high-speed flows [2–7]. This instability leads to a flow-field structure that is dominated by periodic lambda-shaped vortices that are shifted by one half of a wavelength in the spanwise direction and staggered in the streamwise direction. Figure 20 shows a plan view, just below the critical layer, of the total vorticity predicted by the LES with the contraction c_1 and by the fine-grid DNS at $t = 45$. The figure indicates an excellent prediction of the flow structure by LES at this time. The contraction c_2 gives identical results (not shown).

The rope-like wave structure that was observed in high-speed experiments and was explained recently by DNS is associated with the subharmonic secondary instability [10] that is manifested in these computations at the time $t = 45$. This structure is the result of a 2-D projection of the 3-D lambda vortices. The LES is able to capture the rope-like wave structure, even with the coarse grid ($24 \times 12 \times 96$). Figure 21 compares the rope-like structure that is derived from the wall-normal density gradient at $t = 45$ with the corresponding structure from the fine-grid DNS of Pruett and Zang [10] with the $64 \times 36 \times 128$ grid. In Fig. 21 and in the following comparisons with DNS, the DNS grid is filtered to the corresponding LES grid. The significance of Fig. 21 is that although a coarse-grid DNS ($24 \times 12 \times 96$, which is the same as the LES grid) might be able to capture this rope-like structure, LES, with the dynamic model, causes no damping to the flow structure during the early stages of transition as does the standard Smagorinsky model [15].

Following the periodic lambda-shaped vortices, detached high-shear layers of the streamwise velocity are subsequently developed, which ride on top of the lambda vortices. With the intensity of the high-shear layers increasing, they stretch and eventually roll up. Sharp, low-velocity pulses (spikes) are then observed in the peak positions. At several stages in the transition region ($t = 50$, $t = 53$, $t = 54$, and $t = 55$), we compare the flow structure, in terms of the spanwise vorticity that results from LES calculations, with the DNS results [10]. Figures 22–25 show this comparison for both contractions used in the LES calculations. These figures

illustrate several points. First, excellent agreement exists between the LES and DNS results; the LES, with the dynamic model, is able to capture the bulk of the flow structure. Second, both contractions give identical results at the early stages of the transition region (at t = 50, the maximum spanwise vorticity is 4.9 for both contractions, compared with 5.1 for DNS) Third, slight differences in the details of the flow structure begin to occur in the late stages of transition. Fourth, at these late stages of transition, the LES flow-field structure with contraction c_1 compares more favorably with the DNS results.

As the transition process continues, small structures are formed due to the breakdown of the high-shear layer. This results in the periodical appearance of local regions of turbulence in the streamwise and spanwise directions. These regions spread as they travel downstream until a fully turbulent flow is attained. The later developments of the flow field are never understood in high-speed flows because of rare DNS calculations that cover the high computer demand of this stage. In Fig. 26, we present the results of the LES with contraction c_1; these results describe the spanwise vorticity structure of the flow field during the entire transition region and for the beginning of the turbulent region. The figure shows different stages: the formation of the lambda vortices, the development of the high-shear layers, the appearance of spikes, the decay of the large-scale structure, and the formation of new, small structures.

6. CONCLUDING REMARKS

The dynamic eddy-viscosity subgrid-scale model of Germano [27] and Germano et al. [28] has been applied to a high-speed transitional boundary layer at a Mach number of 4.5. In this method, the model coefficients C_r, C_i, and C_θ are determined dynamically as the calculations proceed. The values of the model coefficients are adjusted automatically at different time steps with the local information contained in the resolved flow field.

The application of the dynamic model to a high-speed transitional boundary layer is successful. The model gives the proper asymptotic behavior of the modeled quantities near the wall and in the free stream. The model has no dissipative character like the standard

Smagorinsky model; on the contrary, it turns dynamically off in the linear and early nonlinear regions and on both as the flow approaches the breakdown and in the transition region. The LES with the dynamic model is able to capture the "rope-like" wave structure, even with the coarse grid $24 \times 12 \times 96$.

The LES with the dynamic model is able to capture the bulk of the flow-field structure. While both contractions give identical results at the early stages of the transition region, slight differences in the details of the flow structure occur in the late stages of transition. For these stages, the LES flow-field structure with contraction c_1 compares more favorably with the DNS results.

Large-eddy simulation of transitional flow along a cylinder at Mach 4.5 is achieved with one sixth of the grid resolution that was used for DNS. The structure of the flow field during the entire transition region and the beginning of the turbulent region is demonstrated with LES.

ACKNOWLEDGEMENT

The author appreciates the valuable discussions with Dr. Thomas Zang of NASA Langley Research Center, Dr. David Pruett of Analytical Services & Materials, Inc., and Prof. Ugo Piomelli of the University of Maryland. This work is supported by the Theoretical Flow Physics Branch of NASA Langley Research Center under contract NAS1-19320.

REFERENCES

1. Mack, L. M., Review of Linear Compressible Stability Theory. In Stability for Time Dependent and Spatially Varying Flows, ed. D. L. Dwoyer and M. Y. Hussaini, Springer-Verlag, New York, 1985, pp. 164-187.

2. El-Hady, N. M., Spatial Three-Dimensional Secondary Instability of Compressible Boundary-Layer Flows. AIAA J., vol. 29, no. 5, May 1991, pp. 688-696.

3. El-Hady, N. M., Secondary instability of high-speed flows and the influence of wall cooling and suction. Phys. Fluids A, vol. 4, no. 4, 1992, pp. 727-743.

4. Masad, J. A., and Nayfeh, A. H., Subharmonic Instability of Compressible Boundary Layers. Phys. Fluids A, vol. 2, 1990.

5. Ng, L. L., and Erlebacher, G., Secondary Instabilities in Compressible Boundary Layers. ICASE Report no. 90-58, Phys. Fluids A, vol. 4, 1992, pp. 710-723.

6. Ng., L. L., and Zang, T. A., Secondary instability mechanisms in compressible, axisymmetric boundary layers. AIAA Paper no. 92-0743, 1992.

7. Pruett, C. D., Ng, L. L., and Erlebacher, G., On the nonlinear stability of a high-speed, axisymmetric boundary layer. Phys. Fluids A, vol. 3, no. 12, 1991, pp. 2910-2926.

8. Kendall, J. M., Jr., Wind tunnel experiments relating to supersonic and hypersonic boundary-layer transition. AIAA J., vol. 13, 1975, pp. 290-299.

9. Fischer, M. C., and Weinstein, L. M., Cone transitional boundary layer structure at M_e = 14. AIAA J., vol. 10, no. 5, 1972, pp. 699-701.

10. Pruett, C. D., and Zang, T. A., Direct numerical simulation of laminar breakdown in high-speed, axisymmetric boundary layers. Theoret. Fluid Dynamics, vol. 3, no. 6, 1992, pp. 345-367.

11. Bertolotti, F. P., and Herbert, T., Analysis of the linear stability of compressible boundary layers using the PSE. Theor. Comput. Fluid Dyn., vol. 3, 1991, pp. 117-124.

12. Chang, C.-L., Malik, M. R., Erlebacher, G., and Hussaini, M. Y., Compressible stability of growing boundary layers using parabolized stability equations. AIAA Paper no. 91-1636, 1991.

13. Rogallo, R. S., and Moin, P., Numerical simulation of turbulent flows. Annu. Rev. Fluid Mech., vol. 16, 1984, pp. 99-137.

14. Singer, B. A., Modeling of the transition region. NASA CR 4492, February 1993.

15. Smagorinsky, J., General circulation experiments with the primitive equations. I. The basic experiment. Mon. Weather Rev., vol. 91, 1963, pp. 99-164.

16. Moin, P., and Kim, J., Numerical investigation of turbulent channel flow. J. Fluid Mech., vol. 118, 1982, pp. 381-392.

17. Piomelli, U., and Zang, T. A., Large-eddy simulation of transitional channel flow. Comput. Phys Commun., vol. 65, 1991, pp. 224-230.

18. Piomelli, U., Zang, T. A., Speziale, C. G., and Hussaini, M. Y., On the large eddy simulation of transitional wall-bounded flows. Phys. Fluids A, vol. 2, no. 2, February 1990.

19. Speziale, C. G., Erlebacher, G., Zang, T. A., and Hussaini, M. Y., The subgrid-scale modeling of compressible turbulence. Phys. Fluid, vol. 31, no. 4, April 1988, pp. 940-942.

20. Erlebacher, G., Hussaini, M. Y., Speziale, C. G., and Zang, T. A., Toward the large-eddy simulation of compressible turbulent flows. J. Fluid Mech., vol. 238, 1992, pp. 155-185.

21. Bardina, J., Ferziger, J. H., and Reynolds, W. C., Improved Subgrid-Scale Models for Large-Eddy Simulation. AIAA Paper no. 80-1357, 1980.

22. Zang, T. A., Dahlburg, R. B., and Dahlburg, J. P., Direct and Large-Eddy Simulations of Three-Dimensional Compressible Navier-Stokes Turbulence. Phys. Fluids A, vol. 4, no. 1, 1992, pp. 127-140.

23. Comte, P., Lee, S., and Cabot, W., A subgrid-scale model based on the second order velocity structure function. Center of Turbulence Research, Proc. of the Summer Program 1990, pp. 31-45.

24. Lesieur, M., Comte, P., and Normand, X., Direct and large eddy simulations of transitioning and turbulent shear flows. AIAA Paper no. 91-0335, 1991.

25. Normand, X., and Lesieur, M., Direct and large-eddy simulations of transition in the compressible boundary layer. Theoret. Comput. Fluid Dynamics, vol. 3, 1992, pp. 231-252.

26. Kral, L. D., and Zang, T. A., Large-Eddy Simulation of Supersonic, Wall-Bounded Turbulent Flows. In Transition and Turbulence, Proc. of ICASE/NASA Workshop, Springer-Verlag, 1992.

27. Germano, M., Turbulence: the filtering approach. J. Fluid Mech., vol. 238, 1992, pp. 325-336.

28. Germano, M., Piomelli, U., Moin, P., and Cabot, W., A dynamic subgrid-scale eddy viscosity model. Phys. Fluid A, vol. 3, no. 7, July 1991, pp. 1760-1765.

29. Moin, P., Squires, K., Cabot, W., and Lee, S., A dynamic subgrid-scale model for compressible turbulence and scalar transport. Phys. Fluids A, vol. 3, no. 11, November 1991, pp. 2746-2757.

30. El-Hady, N. M., Zang, T. A., and Piomelli, U., Dynamic subgrid-scale modeling for high-speed transitional boundary layers. In Proc. of Symposium on Engineering Applications of Large-Eddy Simulations, 1993 Fluids Engineering Conference, Washington, D.C., June 20-23, 1993.

31. Piomelli, U., Moin, P., and Ferziger, J. H., Model consistency in large eddy simulation of turbulent channel flows. Phys. Fluids, vol. 31, no. 7, July 1988, pp. 1884-1891.

32. Ronchi, C., Ypma, M., and Canuto, V. M., On the application of the Germano identity to subgrid-scale modeling. Phys. Fluids A, vol. 4, no. 12, 1992, pp. 2927-2929.

33. Ghosal, S., Lund, T. S., and Moin, P., A Dynamic localization model for large-eddy simulation of turbulent flows. CTR Manuscript 139, Stanford University, 1992.

34. Lilly, D. K., A proposed modification of the Germano subgrid scale closure method. Phys. Fluids A, vol. 4, no. 3, 1992, pp. 633-635.

35. Piomelli, U., Cabot, W. H., Moin, P., and Lee, S., Subgrid-scale backscatter in turbulent and transitional flows. Phys. Fluids A, vol. 3, no. 7, 1991, pp. 1766-1771.

36. Erlebacher, G., and Hussaini, M. Y., Numerical experiments in supersonic boundary-layer stability. Phys. Fluids A, vol. 2, no. 1, 1990, pp. 94-104.

37. Pruett, C. D., and Streett, C. L., A spectral collocation method for compressible, nonsimilar boundary layers. Int. J. Numer. Meth. Fluids, vol. 13, no. 6, 1991, pp. 713-737.

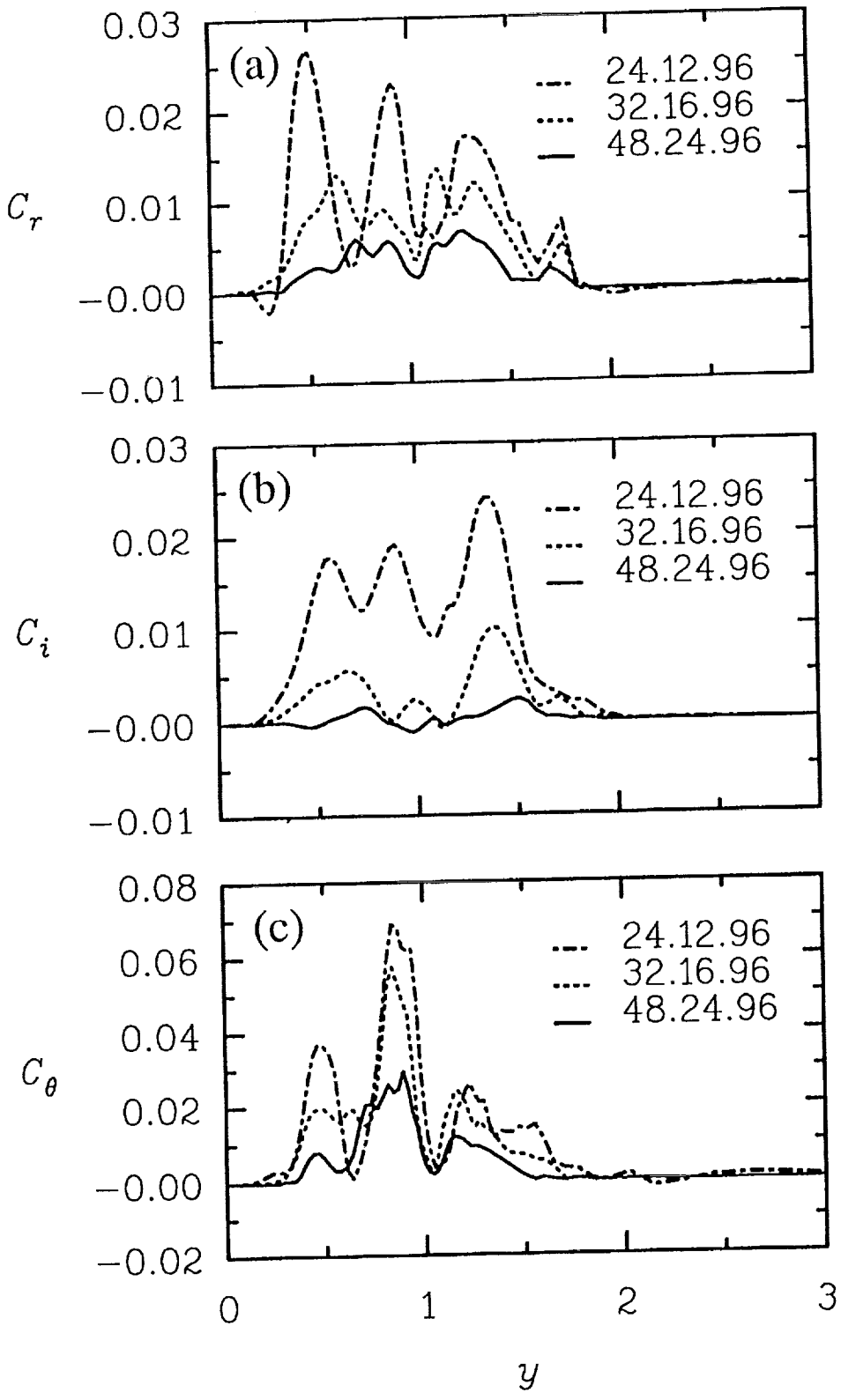

Figure 1. Effect of filter width on plane-averaged coefficients of dynamic model at t = 54 (inside transition region) with contraction c_1: (a) C_r, (b) C_i, and (c) C_θ.

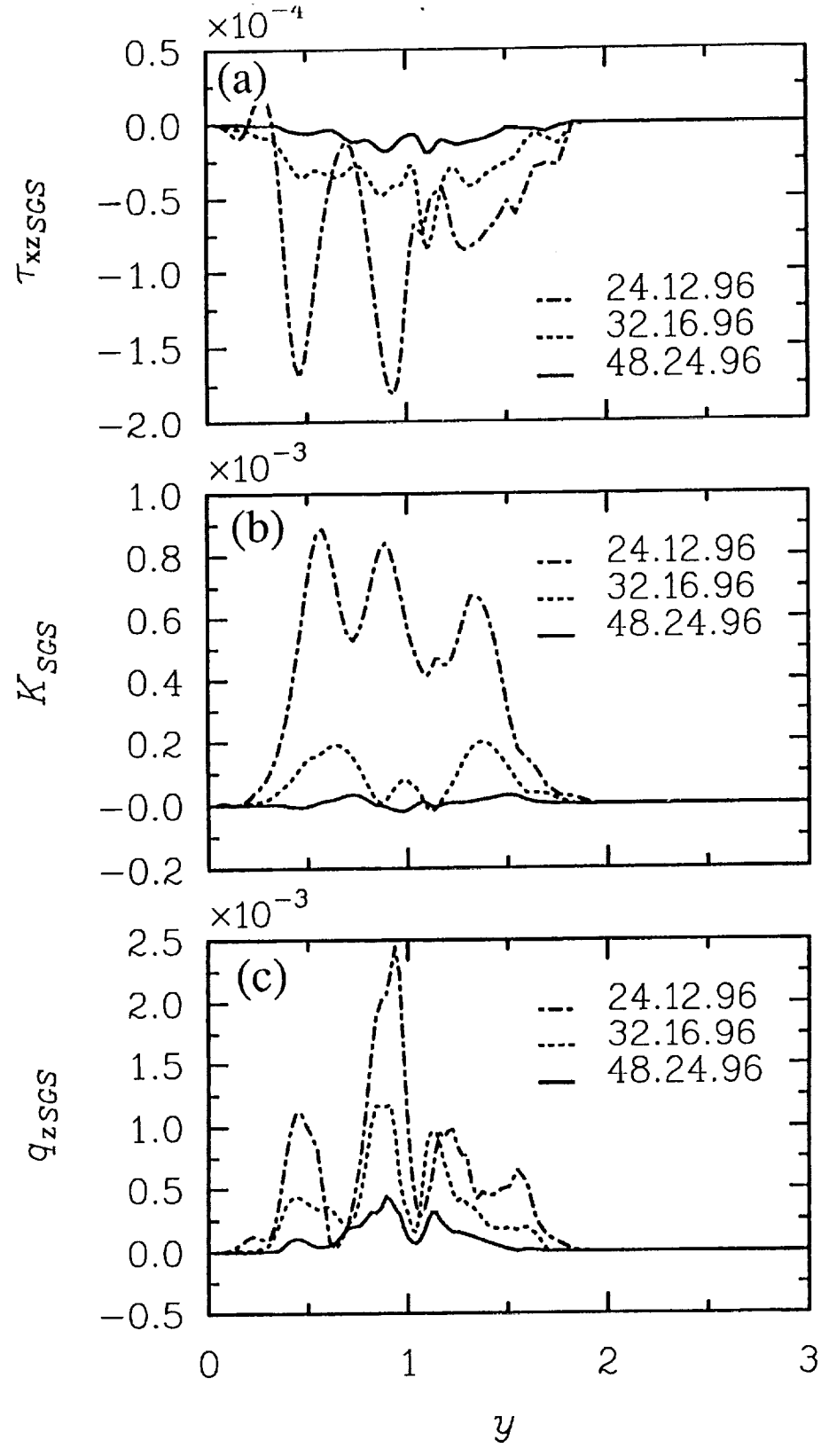

Figure 2. Effect of filter width on plane-averaged (a) component τ_{xz} of SGS stress tensor, (b) SGS kinetic energy, and (c) component q_z of heat flux vector at t = 54 with contraction c_1.

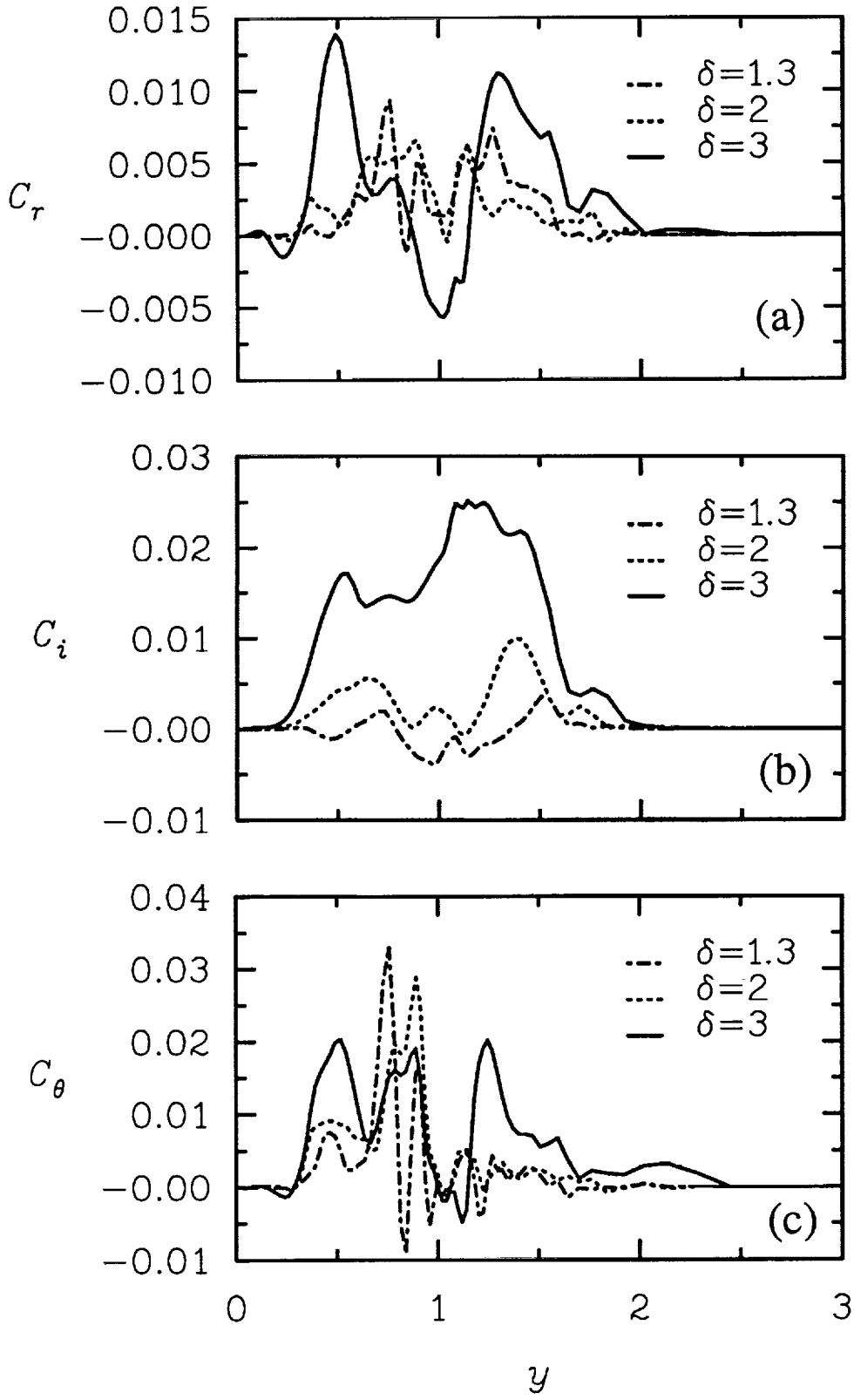

Figure 3. Effect of ratio δ on plane-averaged coefficients of dynamic model at t = 54 (inside transition region) with contraction c_2: (a) C_r, (b) C_i, and (c) C_θ.

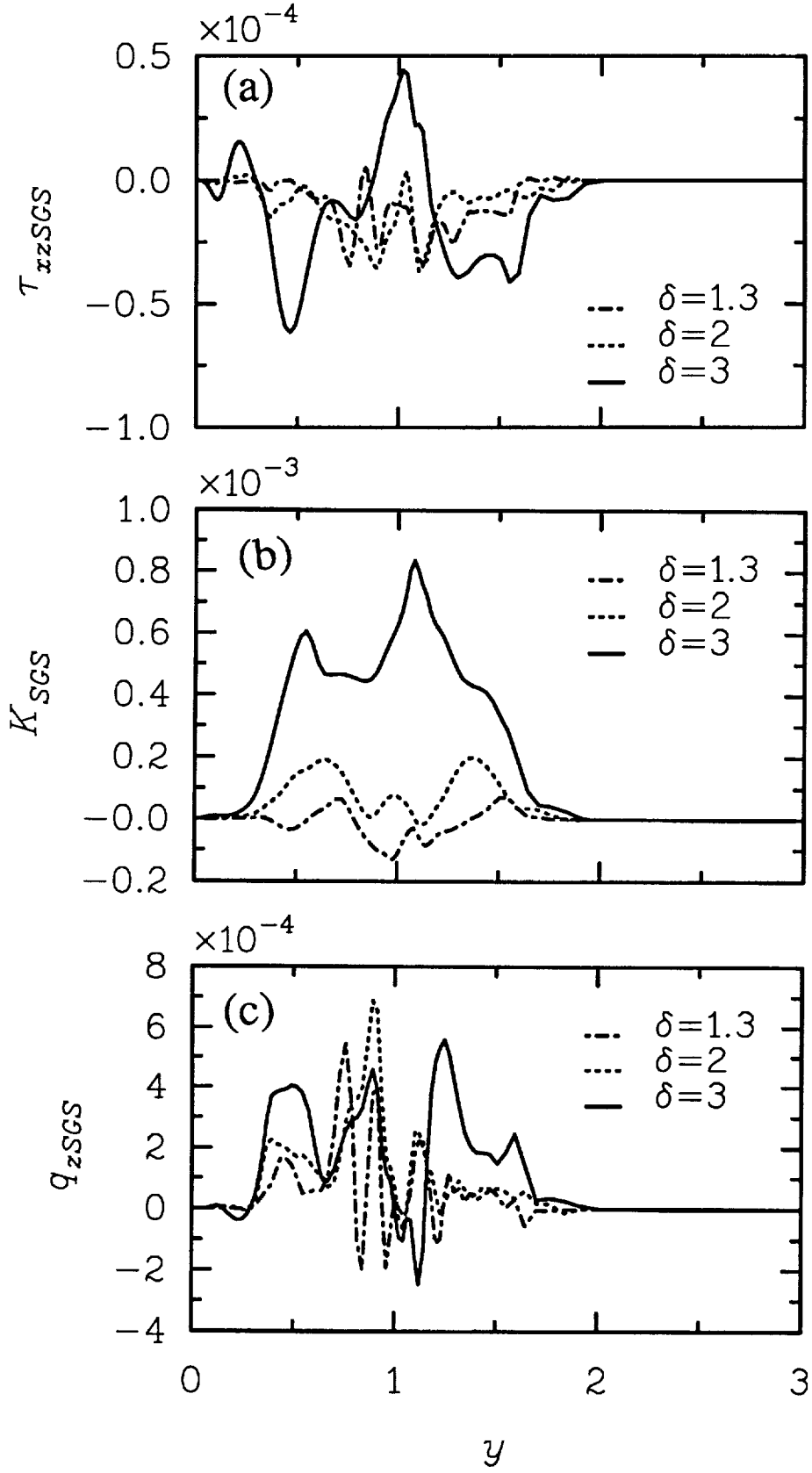

Figure 4. Effect of ratio δ on plane-averaged (a) component τ_{xz} of SGS stress tensor, (b) SGS kinetic energy, and (c) component q_z of heat flux vector at t = 54 with contraction c_2.

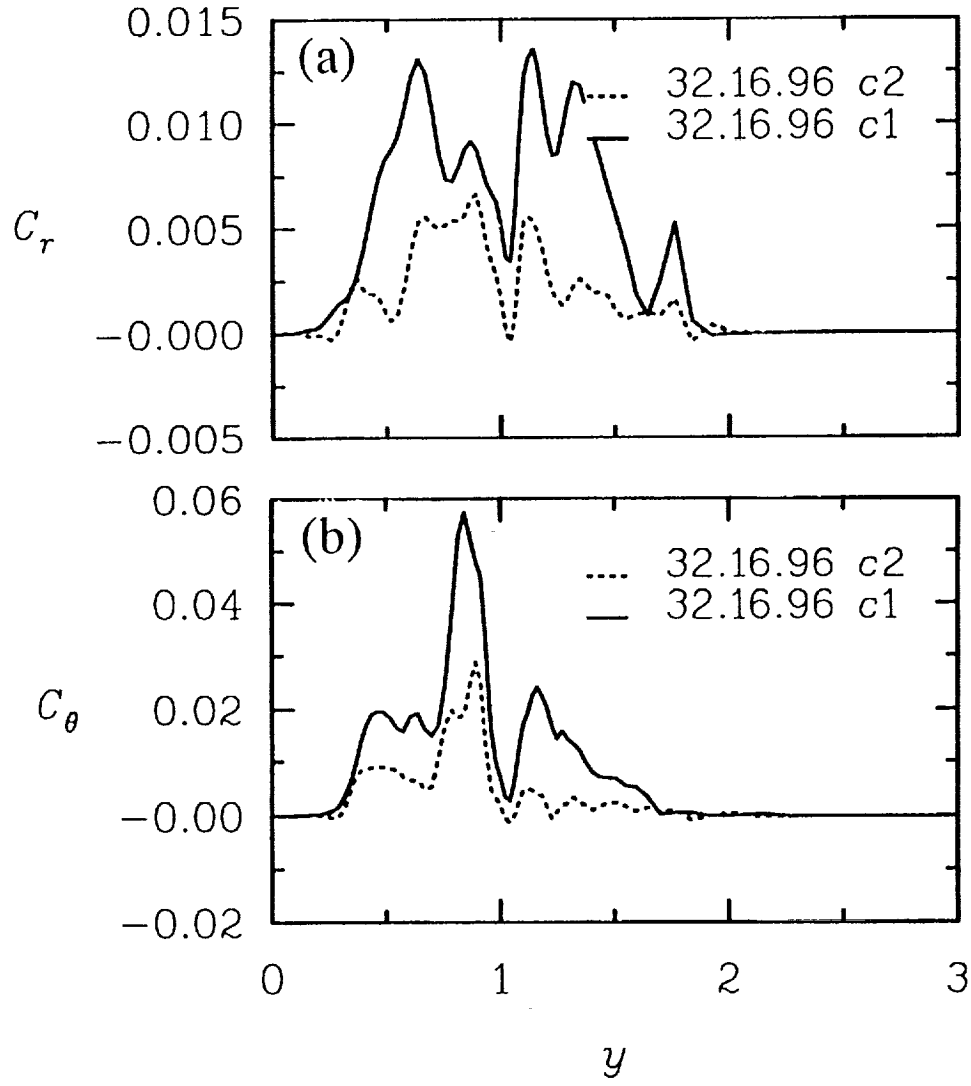

Figure 5. Effect of different contractions on plane-averaged coefficients of dynamic model for grid filter 32 × 16 × 96 at t = 54: (a) C_r, (b) C_θ.

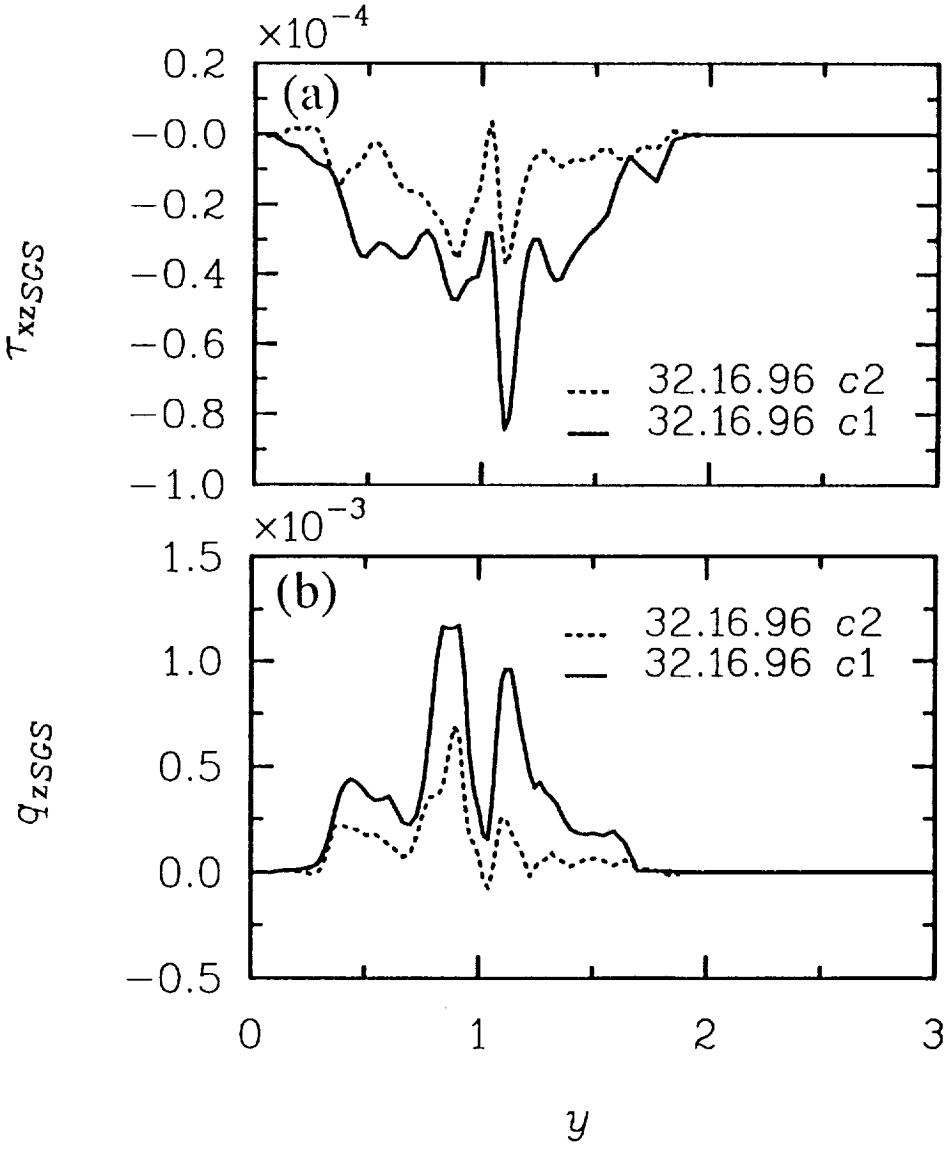

Figure 6. Effect of different contractions on plane-averaged (a) component τ_{xz} of the SGS stress tensor and (b) component q_z of heat flux vector for grid filter 32 × 16 × 96 at t = 54.

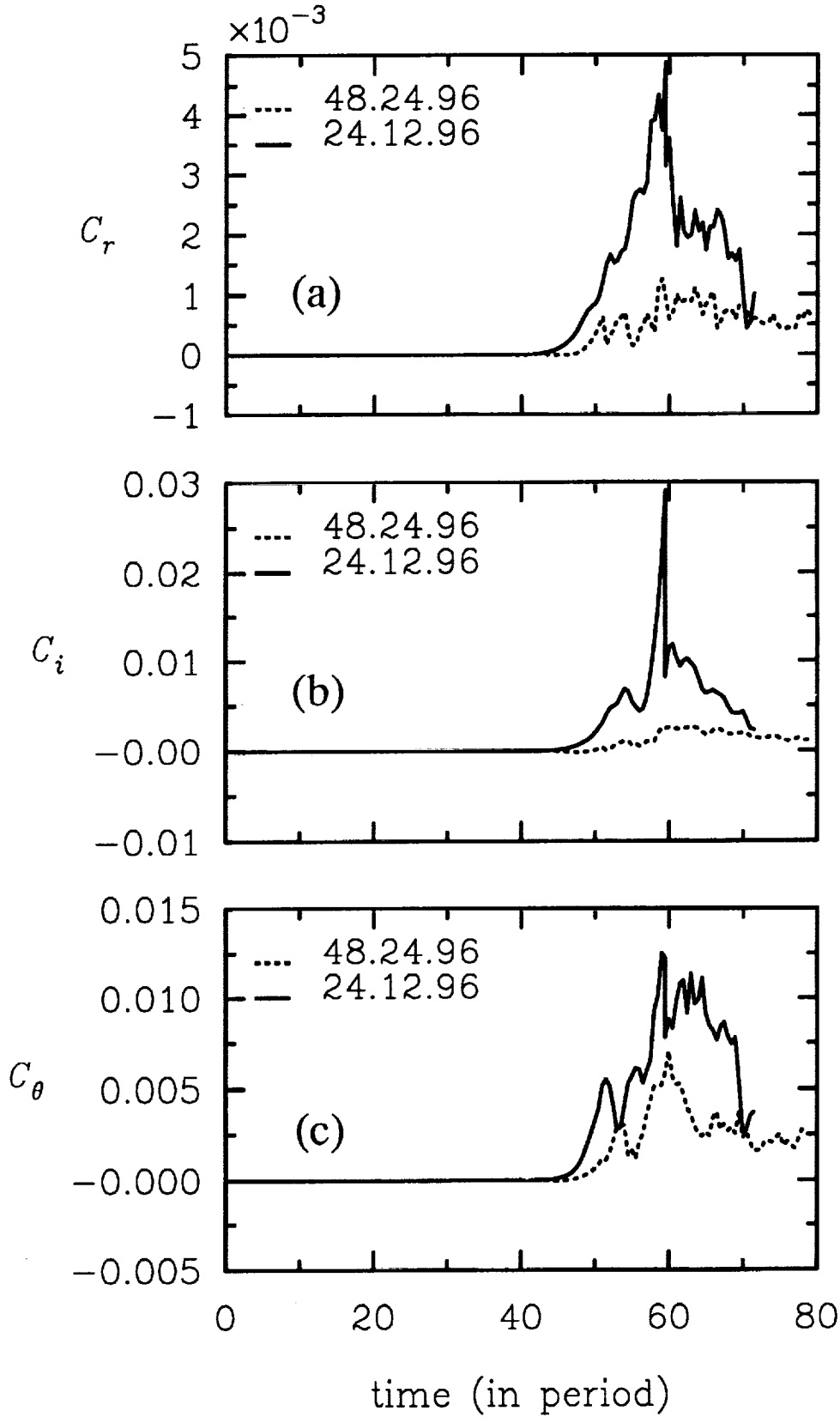

Figure 7. Evolution in time of plane-averaged coefficients of dynamic model with contraction c_2: (a) C_r, (b) C_i, and (c) C_θ. Coefficients are averaged in wall-normal direction for this graph.

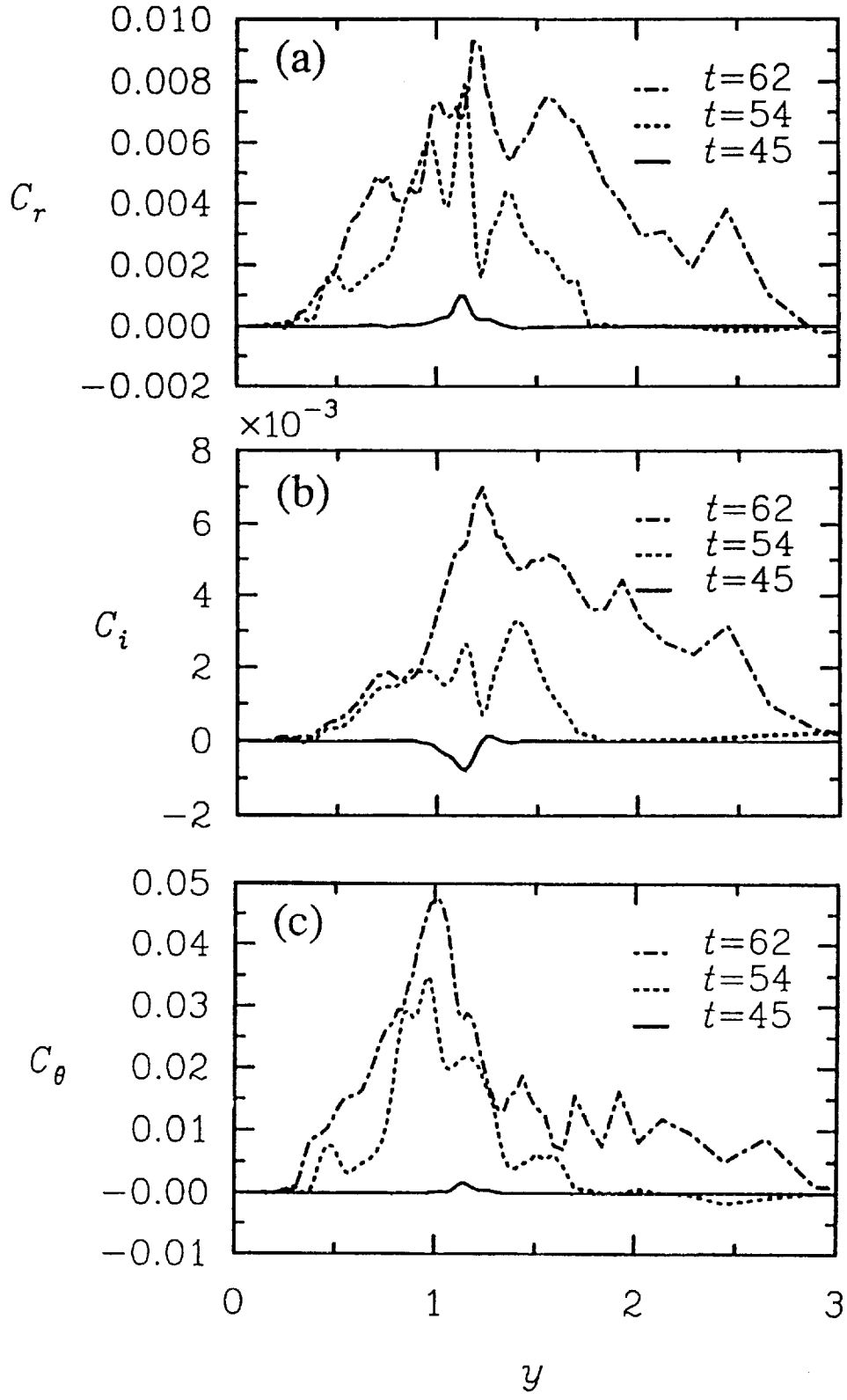

Figure 8. Evolution in time of the normal to wall distribution of plane-averaged coefficients of dynamic model with contraction c_1: (a) C_r, (b) C_i, and (c) C_θ.

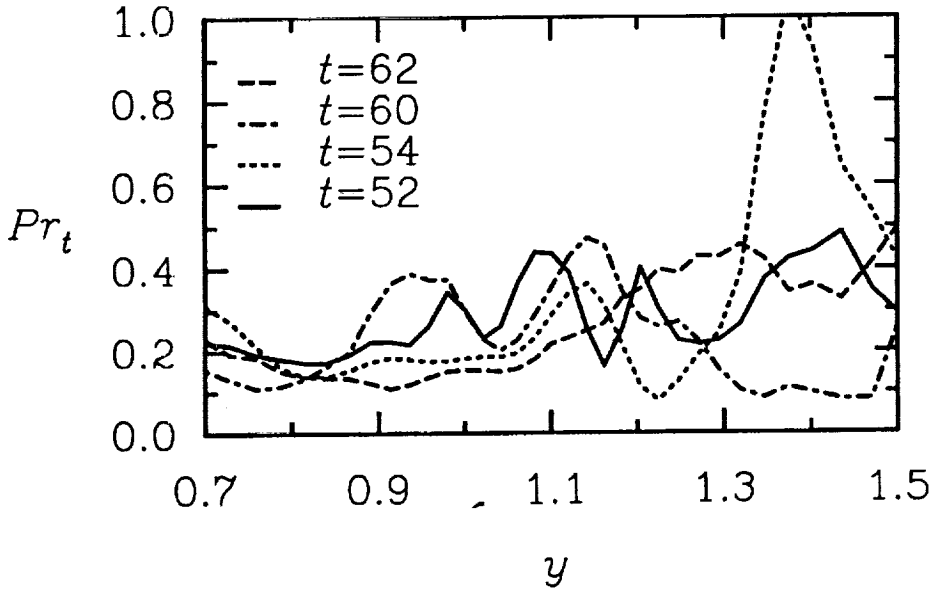

Figure 9. Evolution in time of the normal to wall distribution of plane-averaged turbulent Prandtl number Pr_t with contraction c_1.

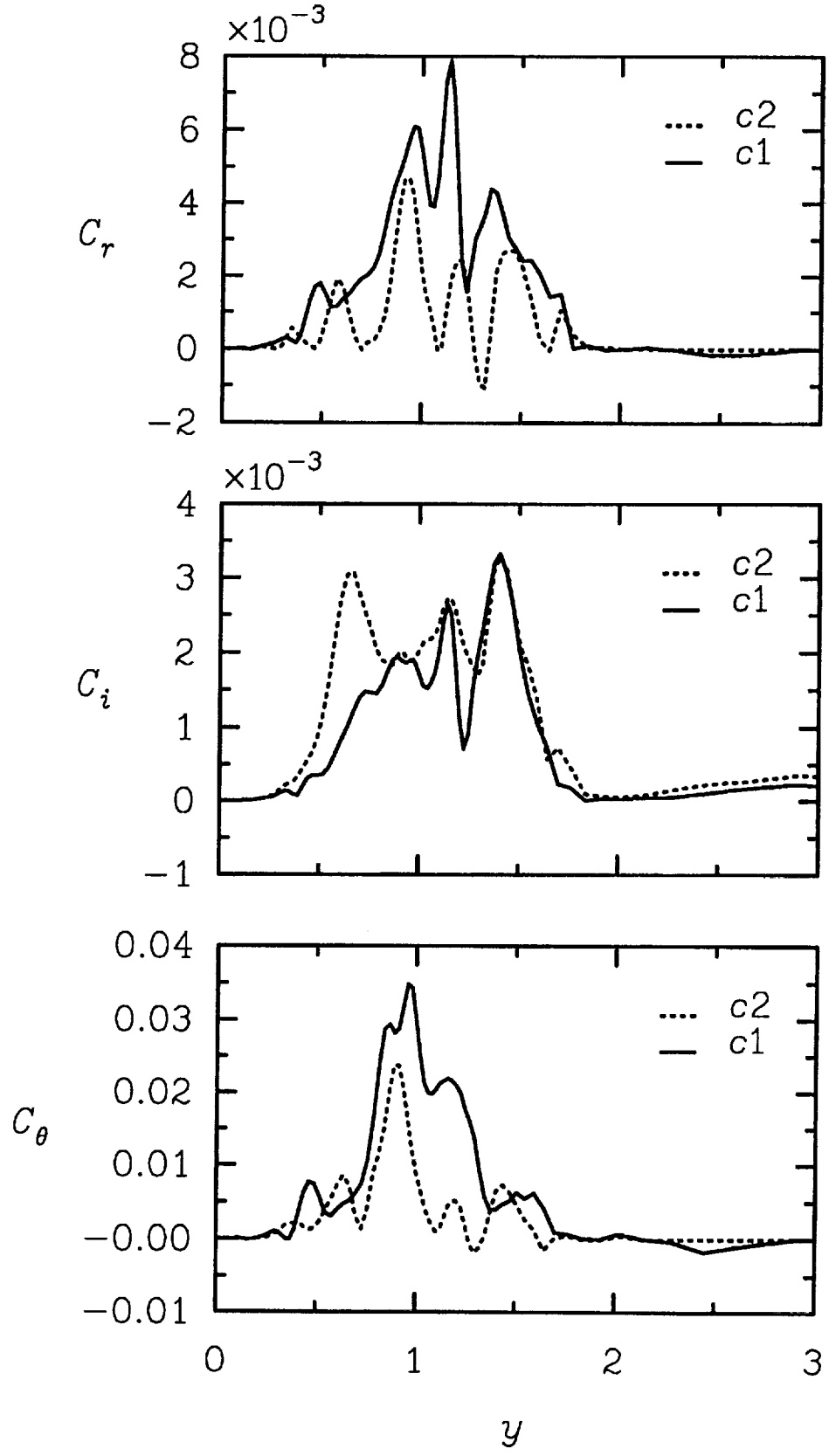

Figure 10. Effect of different contractions on plane-averaged coefficients of dynamic model in large-eddy simulation with grid 48 × 24 × 96 at t = 54: (a) C_r, (b) C_i, (c) C_θ.

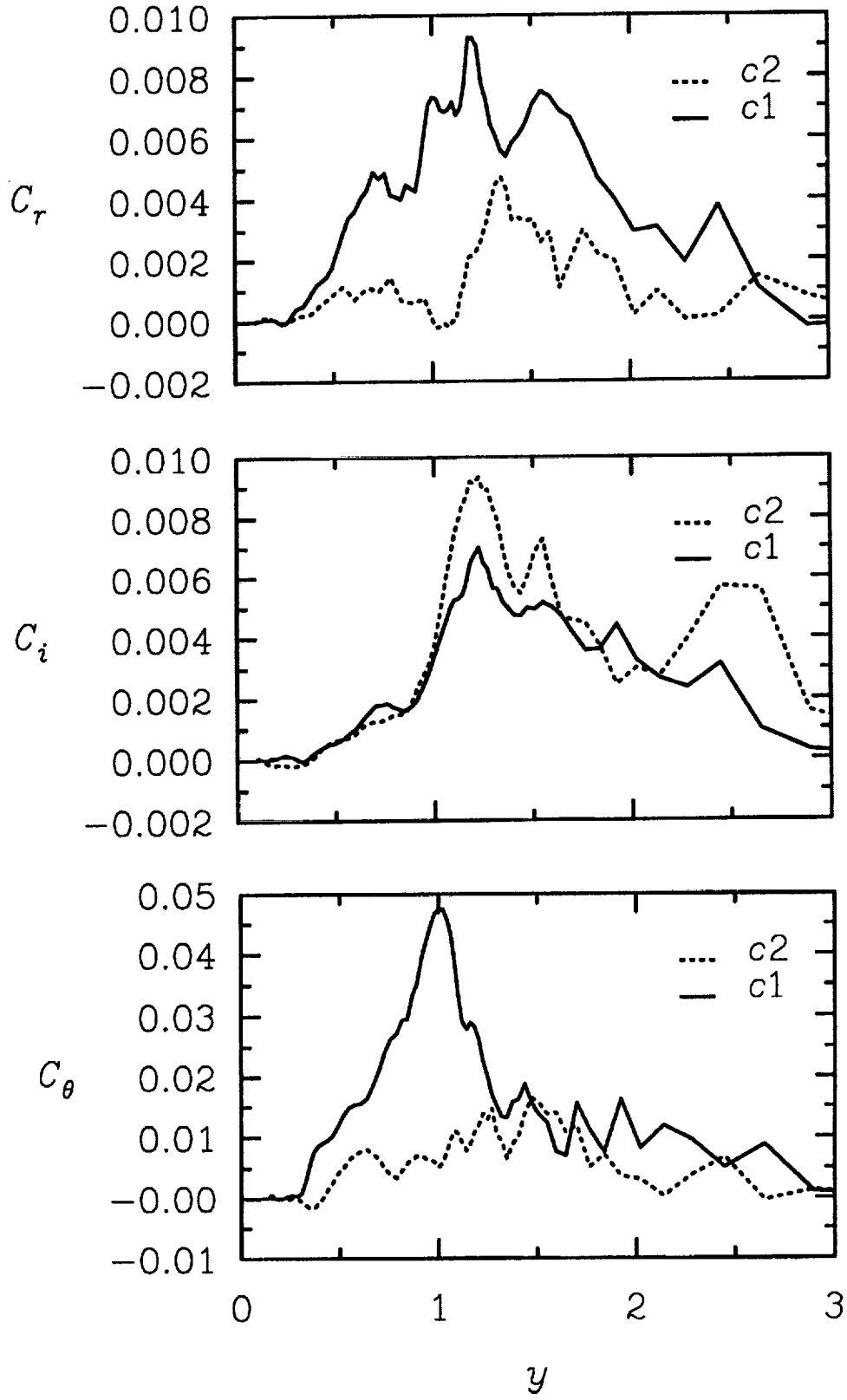

Figure 11. Effect of different contractions on plane-averaged coefficients of dynamic model in large-eddy simulation with grid 48 × 24 × 96 at t = 62: (a) C_r, (b) C_i, (c) C_θ.

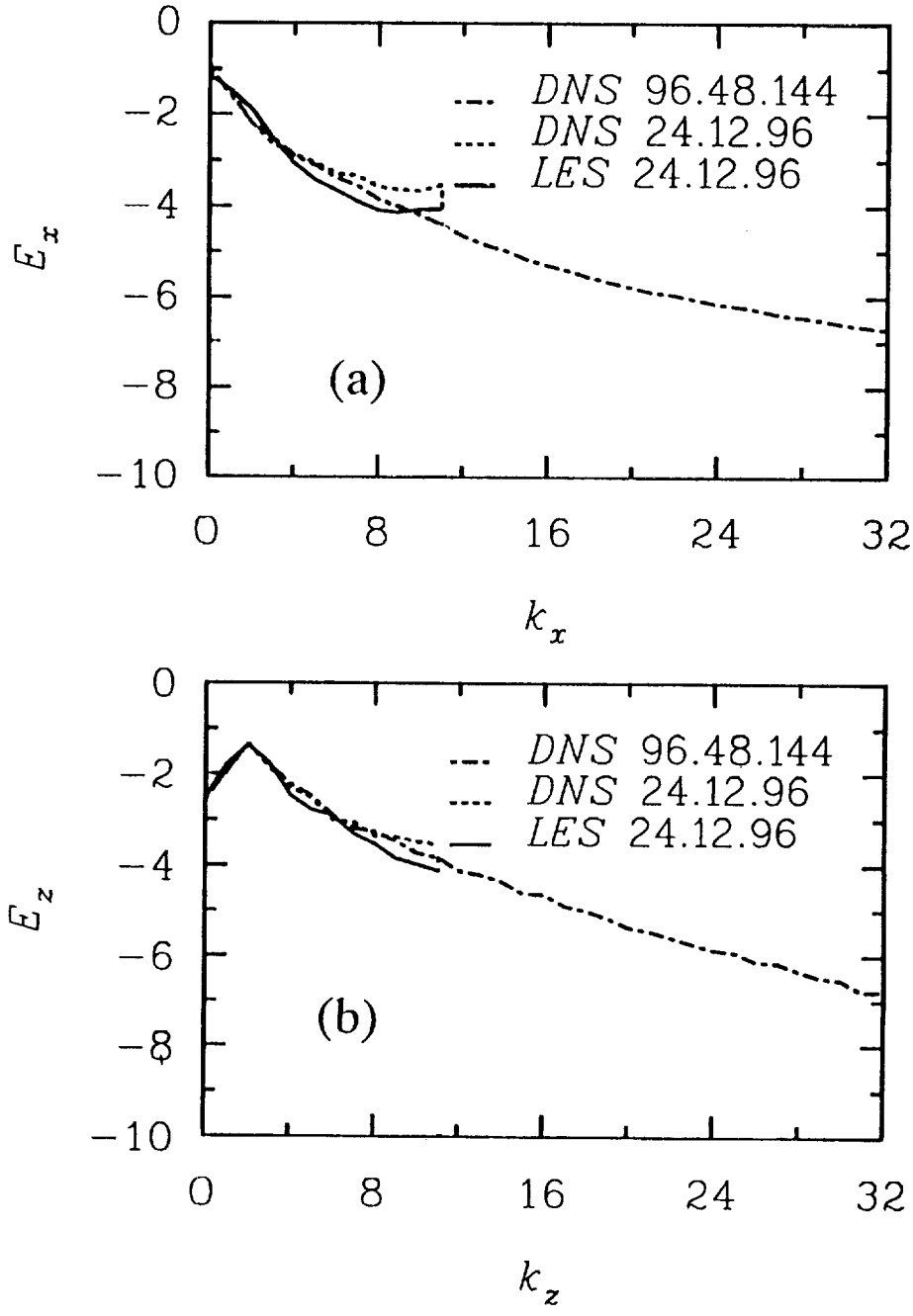

Figure 12. One-dimensional spectra of flow kinetic energy at t = 55 for 24 × 12 × 96 LES with contraction c_1: (a) streamwise spectra and (b) spanwise spectra.

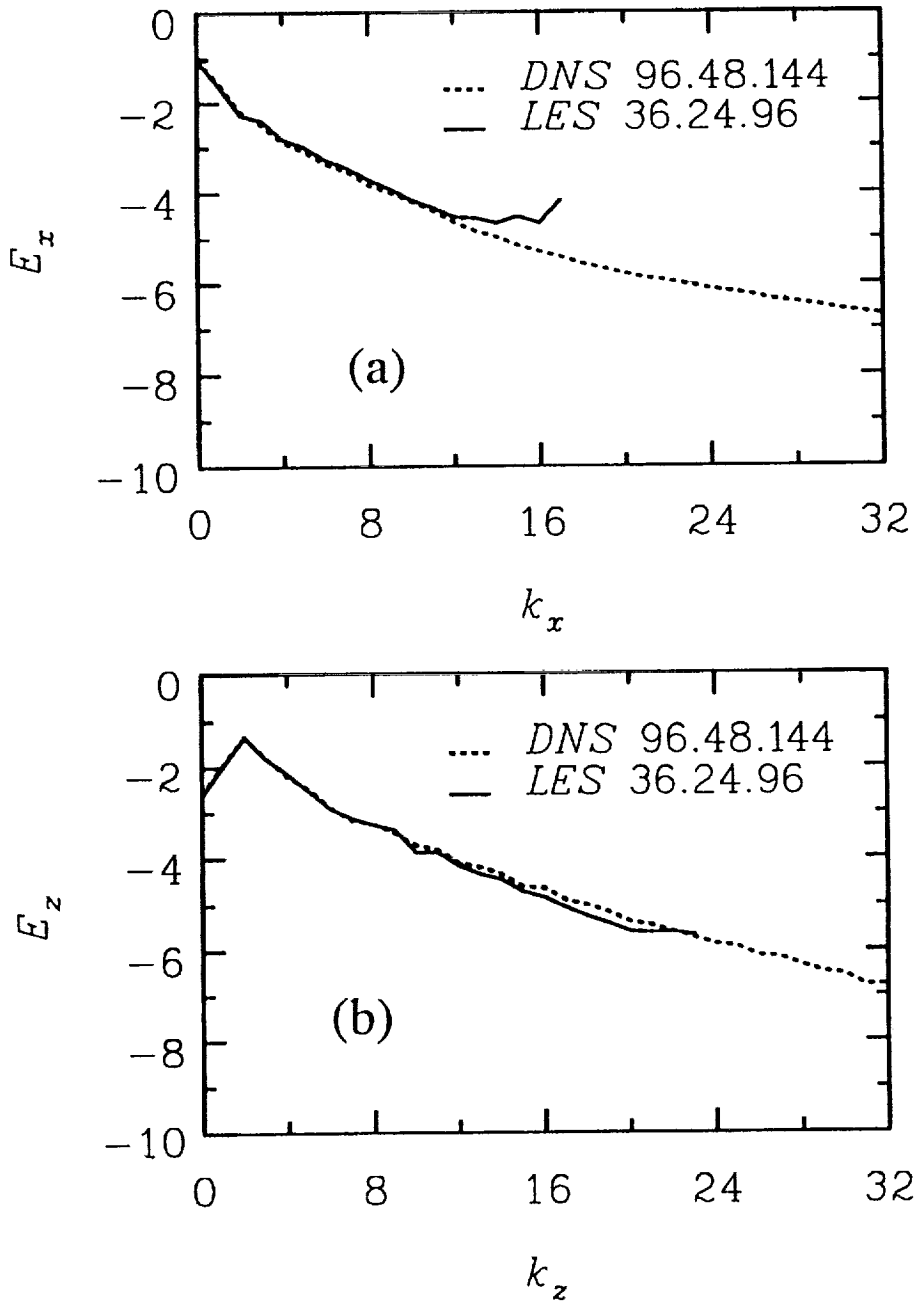

Figure 13. One-dimensional spectra of flow kinetic energy at t = 55 for 48 × 24 × 96 LES with contraction c_1: (a) streamwise spectra and (b) spanwise spectra.

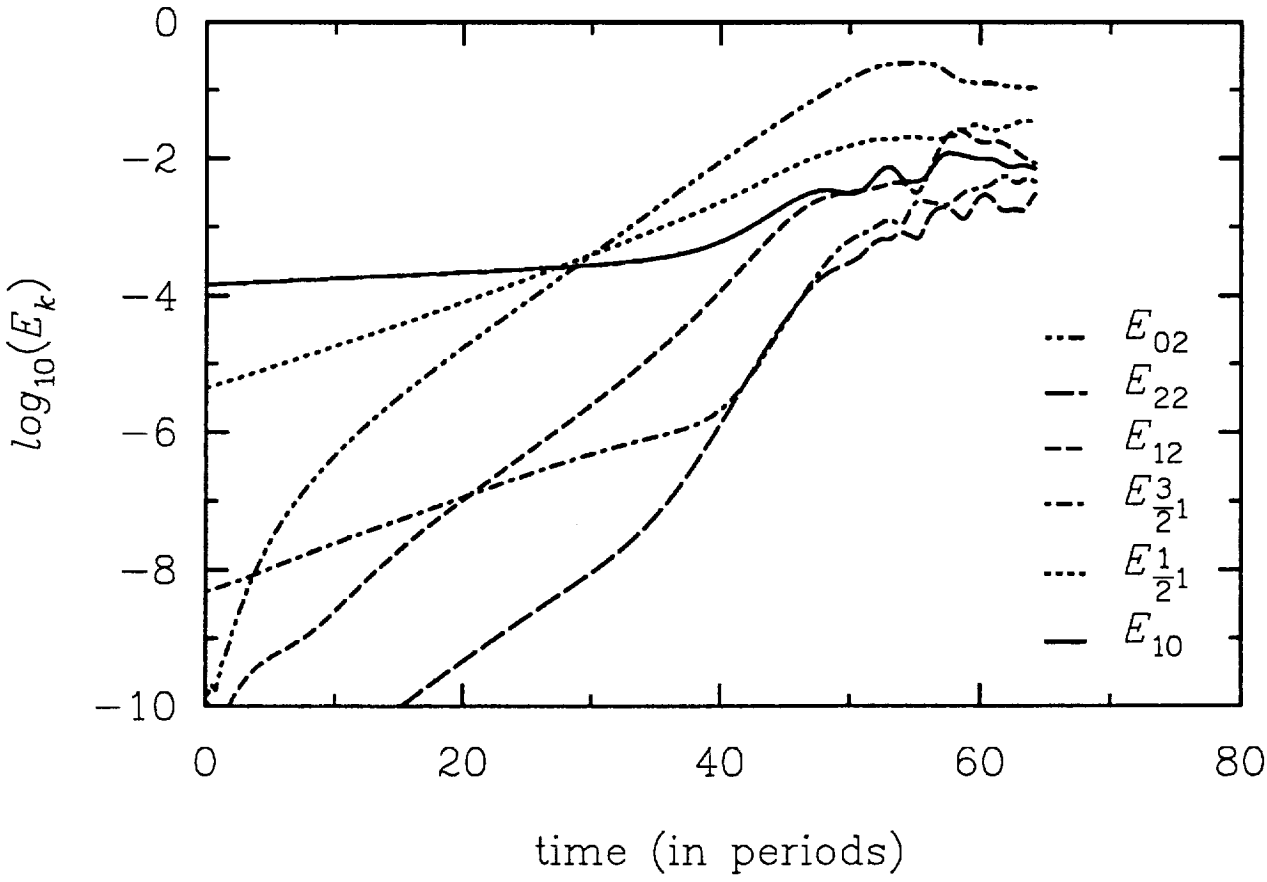

Figure 14. Evolution in time of principal Fourier harmonics in terms of energy content for LES with final grid $48 \times 24 \times 96$ and contraction c_1.

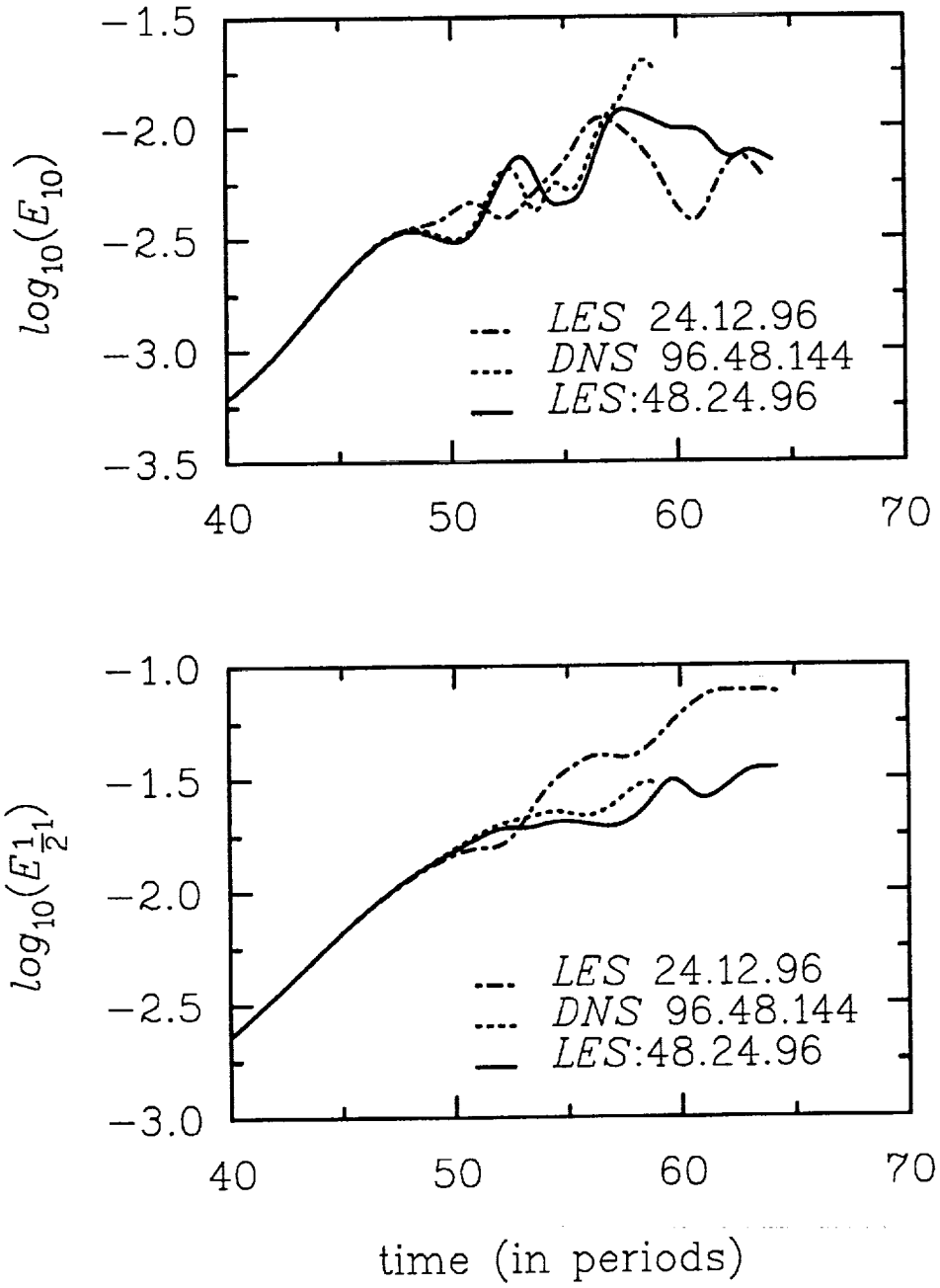

Figure 15. Comparison of time evolution of energy content of Fourier harmonics (1,0), (1/2,1) inside transition region between LES (24 × 12 × 96), LES (48 × 24 × 96), with contraction c_1 and fine-grid DNS (96 × 48 × 144) [10].

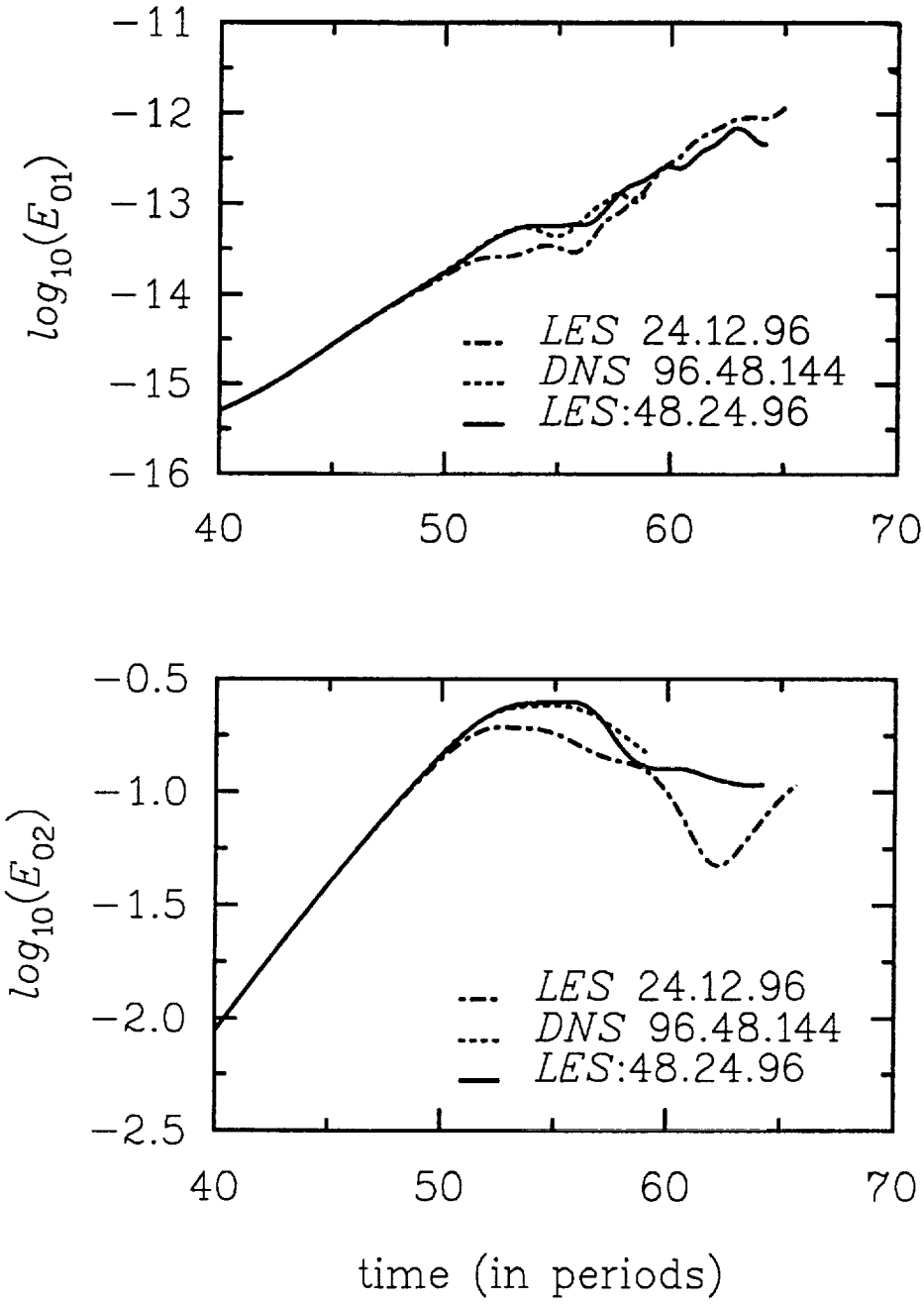

Figure 16. Comparison of time evolution of energy content of Fourier harmonics (0,1), and (0,2) inside the transition region between LES (24 × 12 × 96), LES (48 × 24 × 96), with contraction c_1 and fine-grid DNS (96 × 48 × 144) [10].

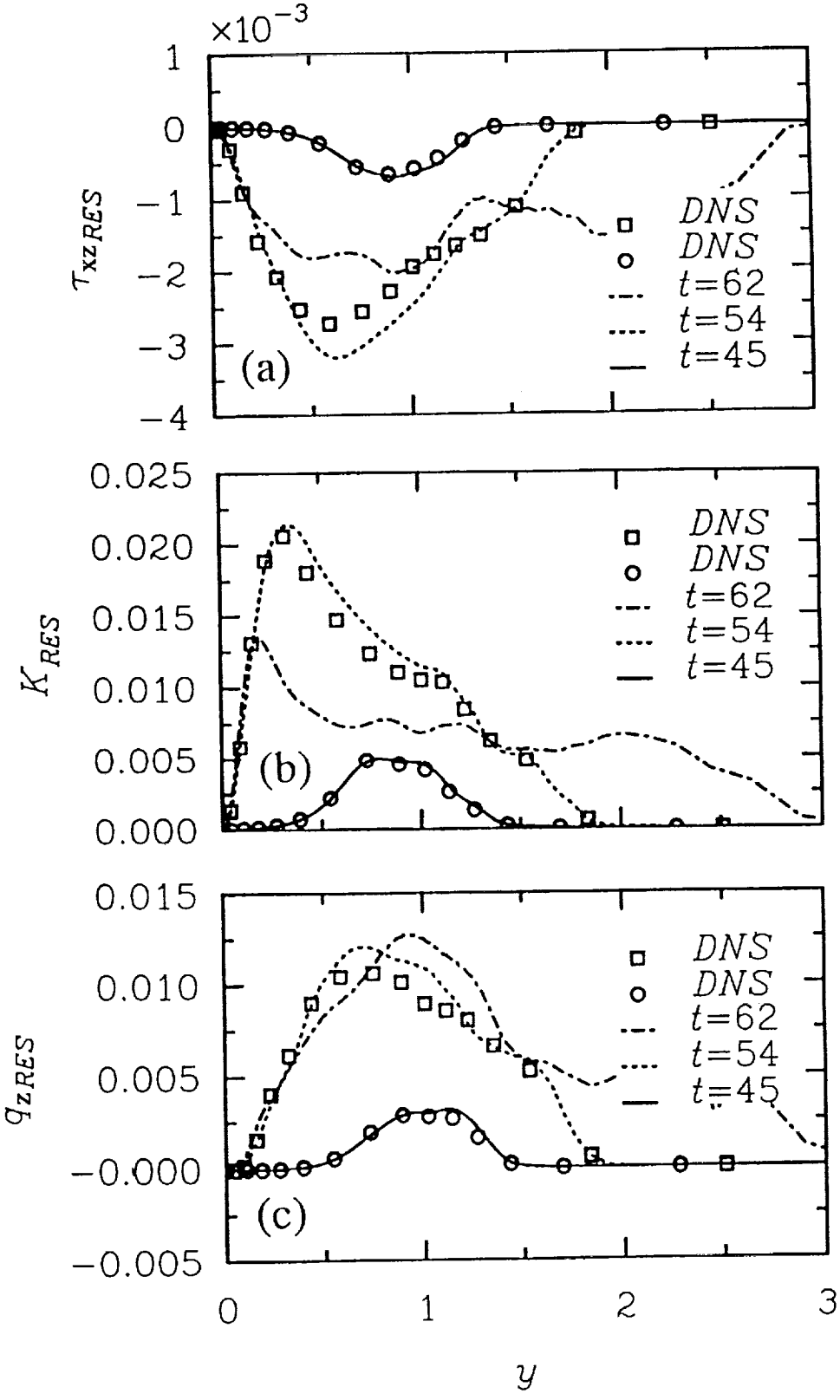

Figure 17. Evolution with time of large-scale field (resolved) with contraction c_1 in terms of plane-averaged (a) Reynolds stress component τ_{xz}, (b) kinetic energy K, and (c) heat flux component q_z.

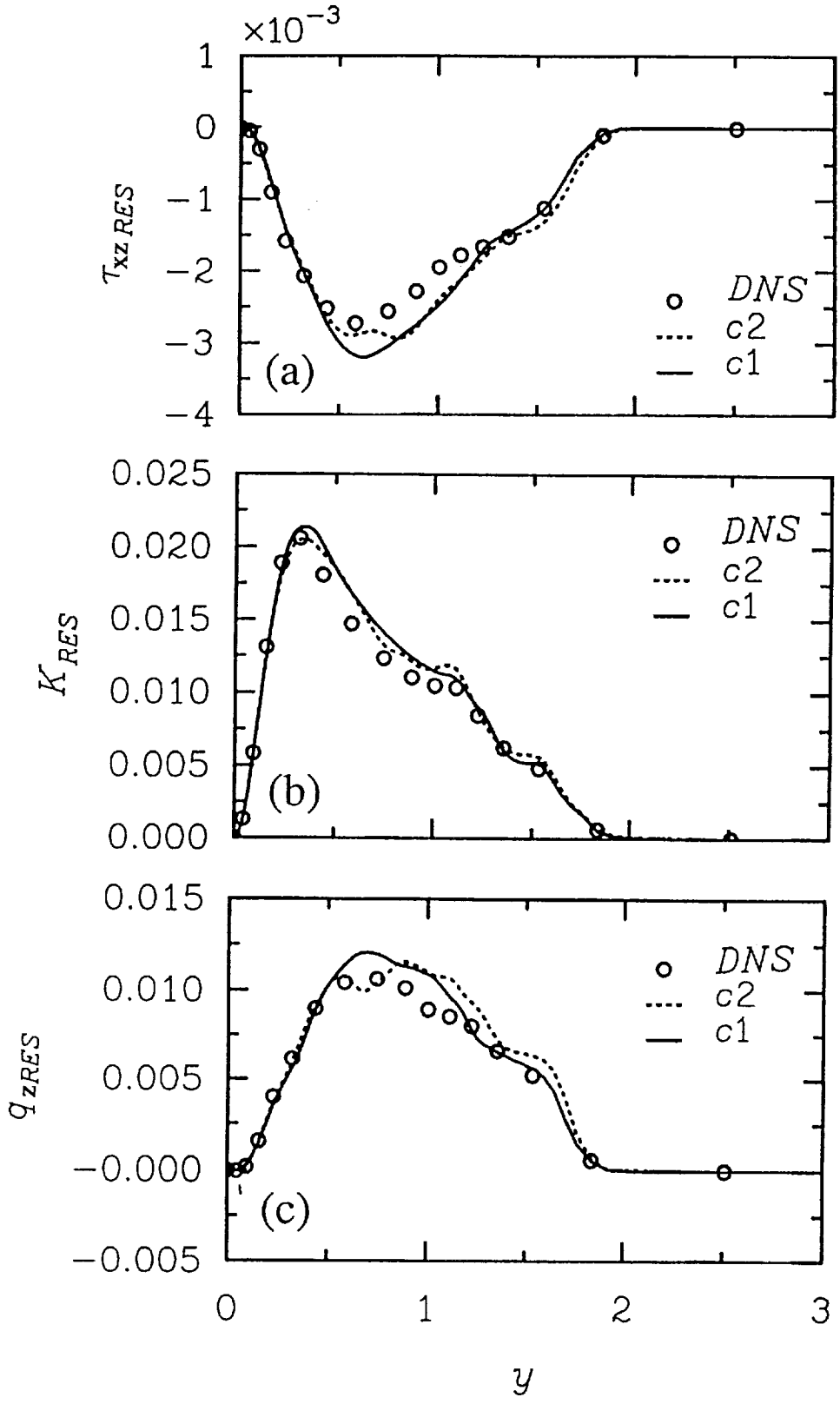

Figure 18. Comparison of large scale results (resolved) at t = 54 with contractions c_1 and c_2 and fine-grid DNS results: (a) Reynolds stress component τ_{xz}, (b) kinetic energy K, and (c) heat flux component q_z.

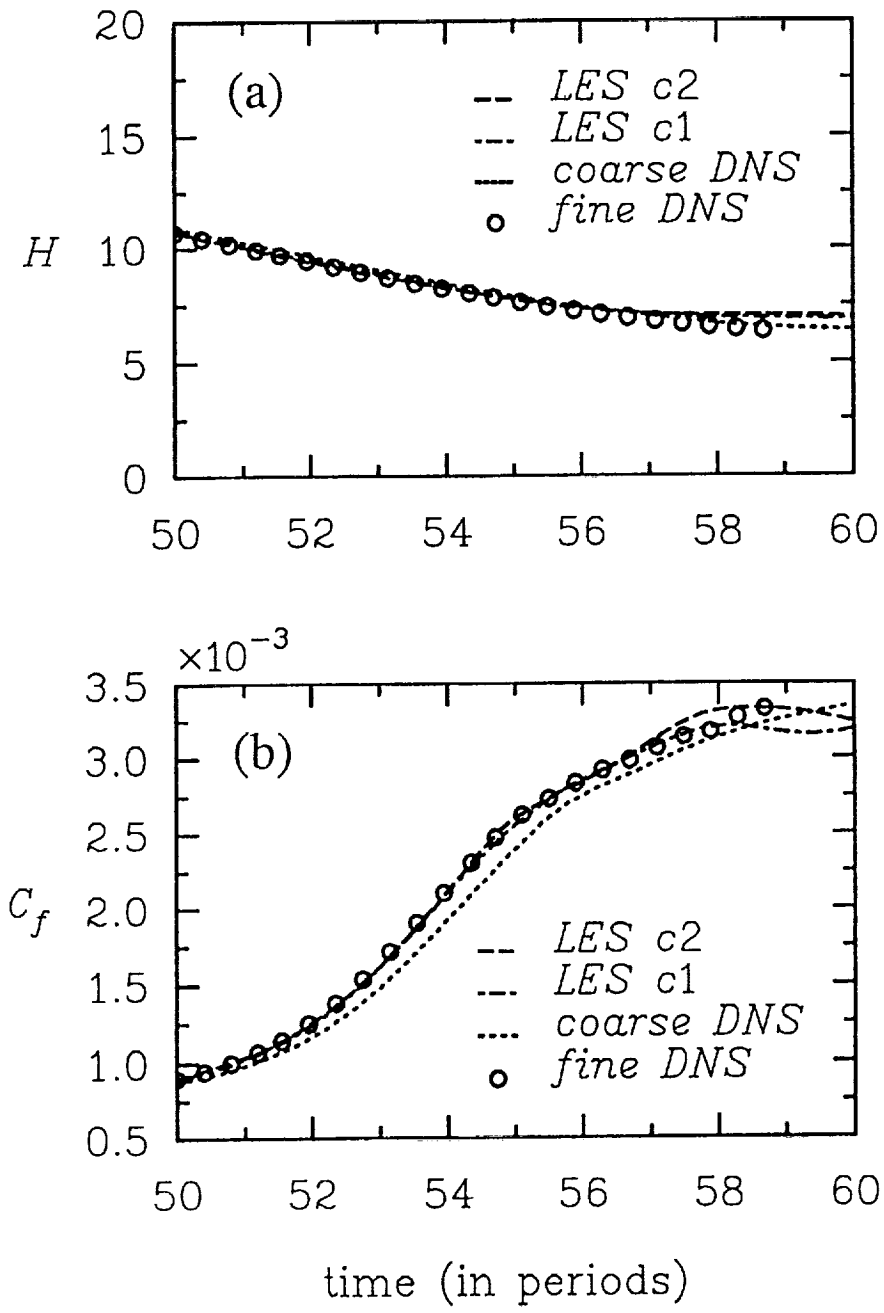

Figure 19. Comparison of time development of (a) the shape factor H and (b) the skin friction C_f with contractions c_1 and c_2 with both fine- and coarse-grid DNS results.

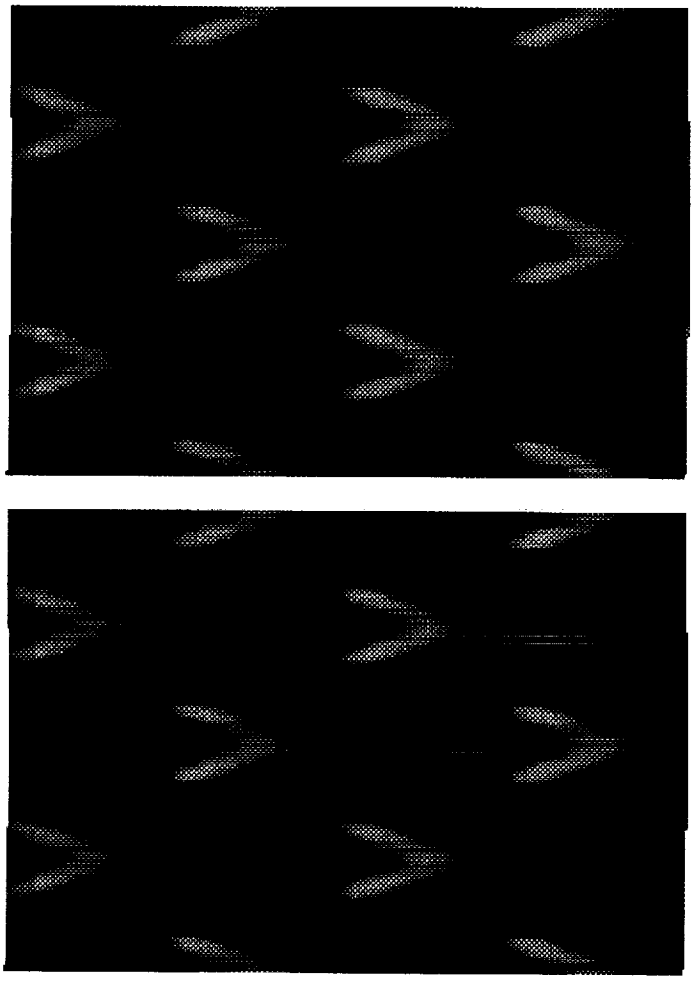

Figure 20. Comparison of total vorticity (plan view just below the critical layer) at t = 45 between LES and DNS with fine grid [10].

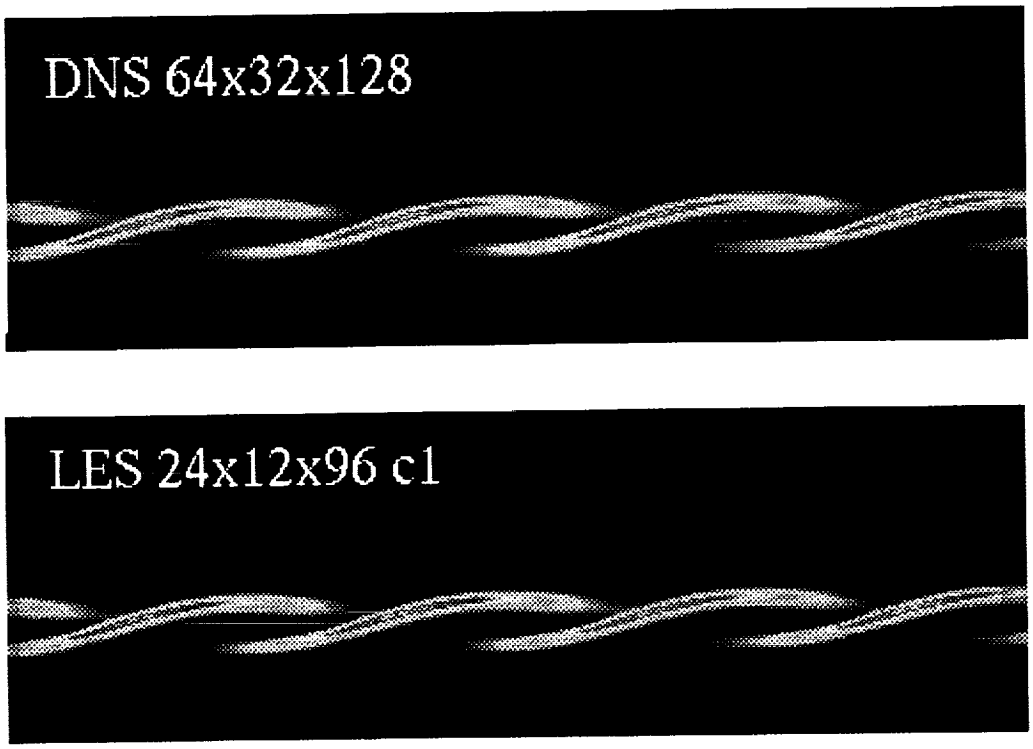

Figure 21. Rope-like structure derived from wall-normal density gradient at $t = 45$ for LES with grid $24 \times 12 \times 96$ compared with corresponding structure from DNS with fine grid [10].

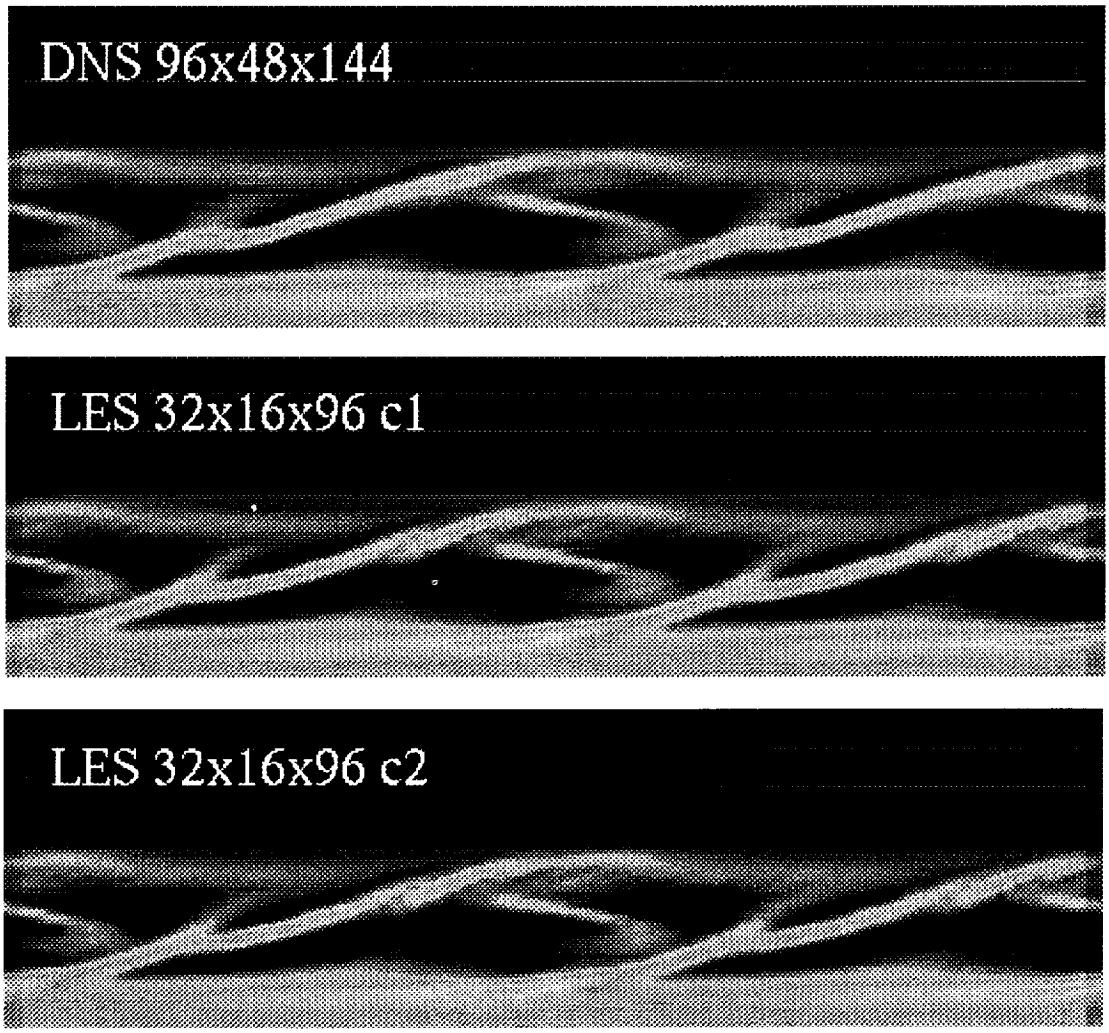

Figure 22. Comparison of spanwise component of vorticity at t = 50 between LES and DNS with fine grid [10].

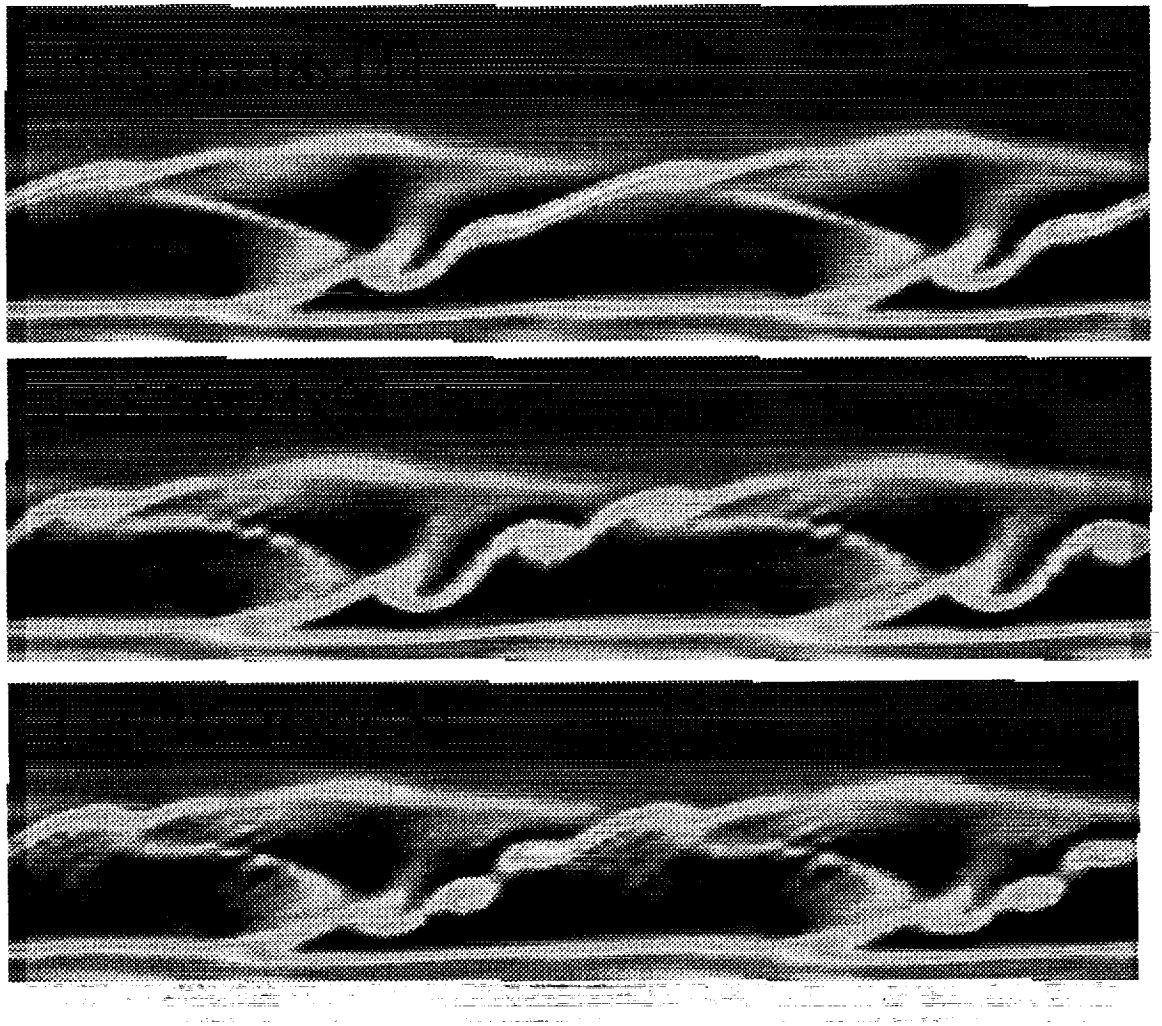

Figure 23. Comparison of spanwise component of vorticity at t = 53 between LES and DNS with fine grid [10].

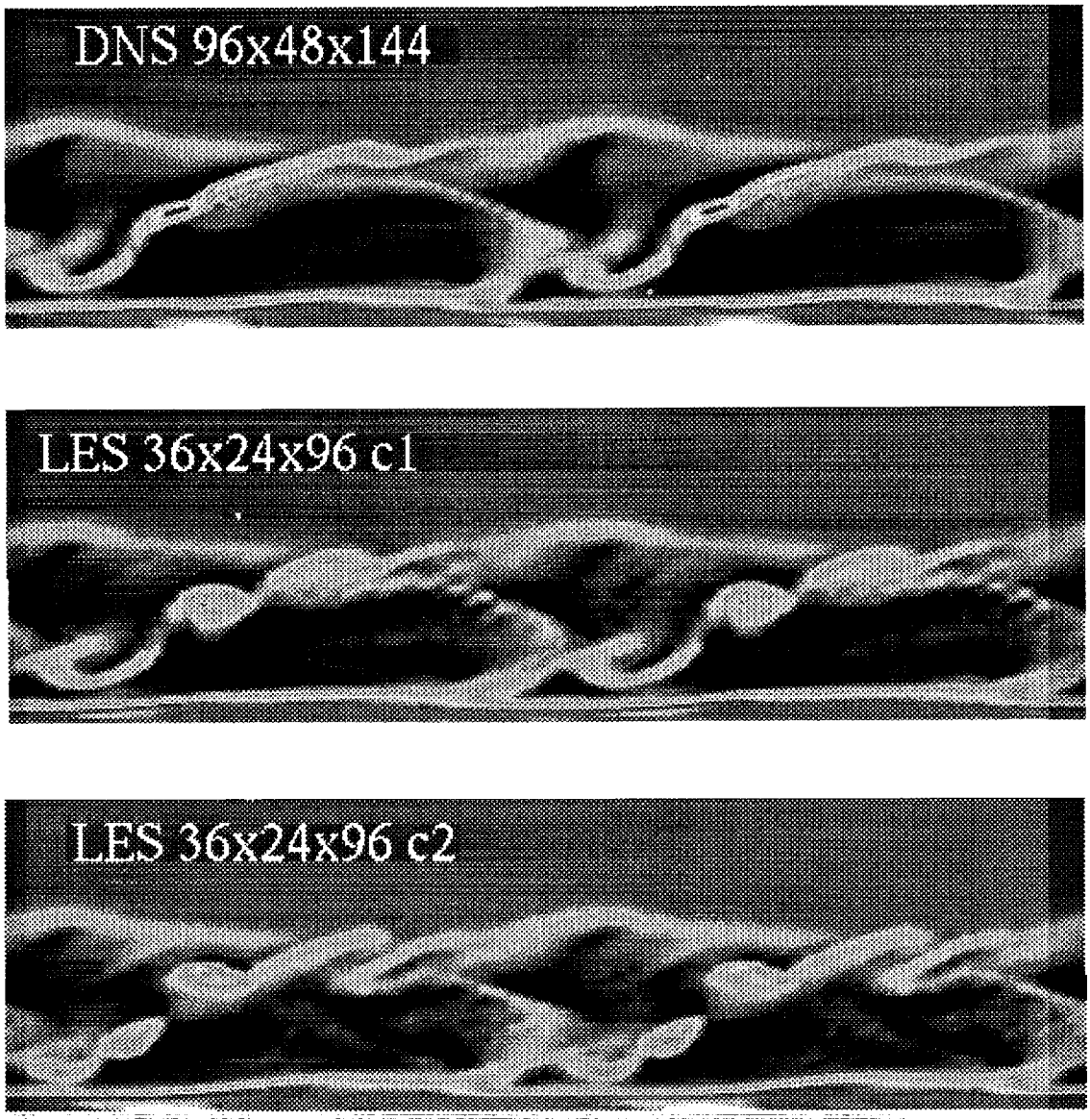

Figure 24. Comparison of spanwise component of vorticity at t = 54 between LES and DNS with fine grid [10].

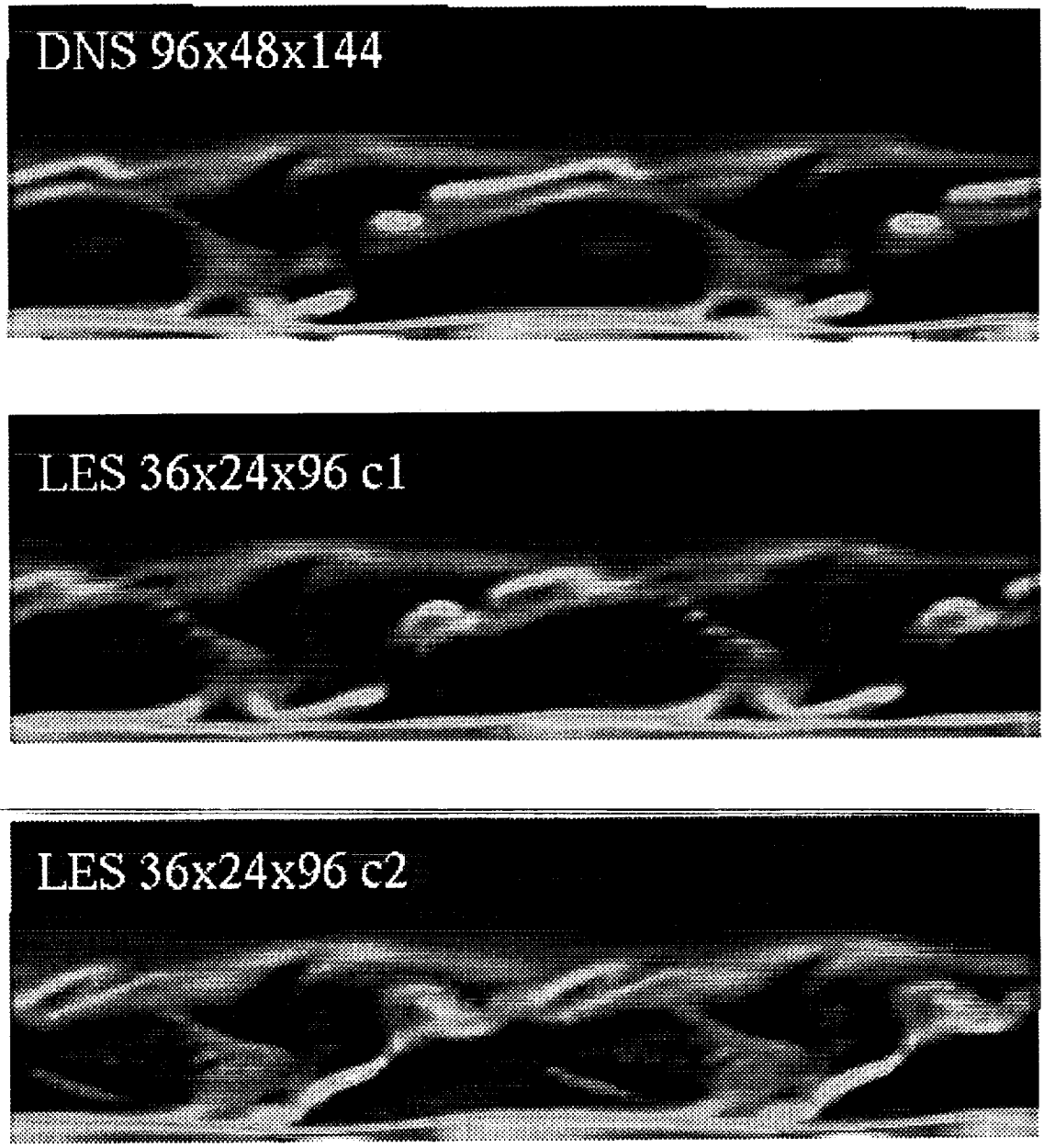

Figure 25. Comparison of spanwise component of vorticity at t = 55 between LES and DNS with fine grid [10].

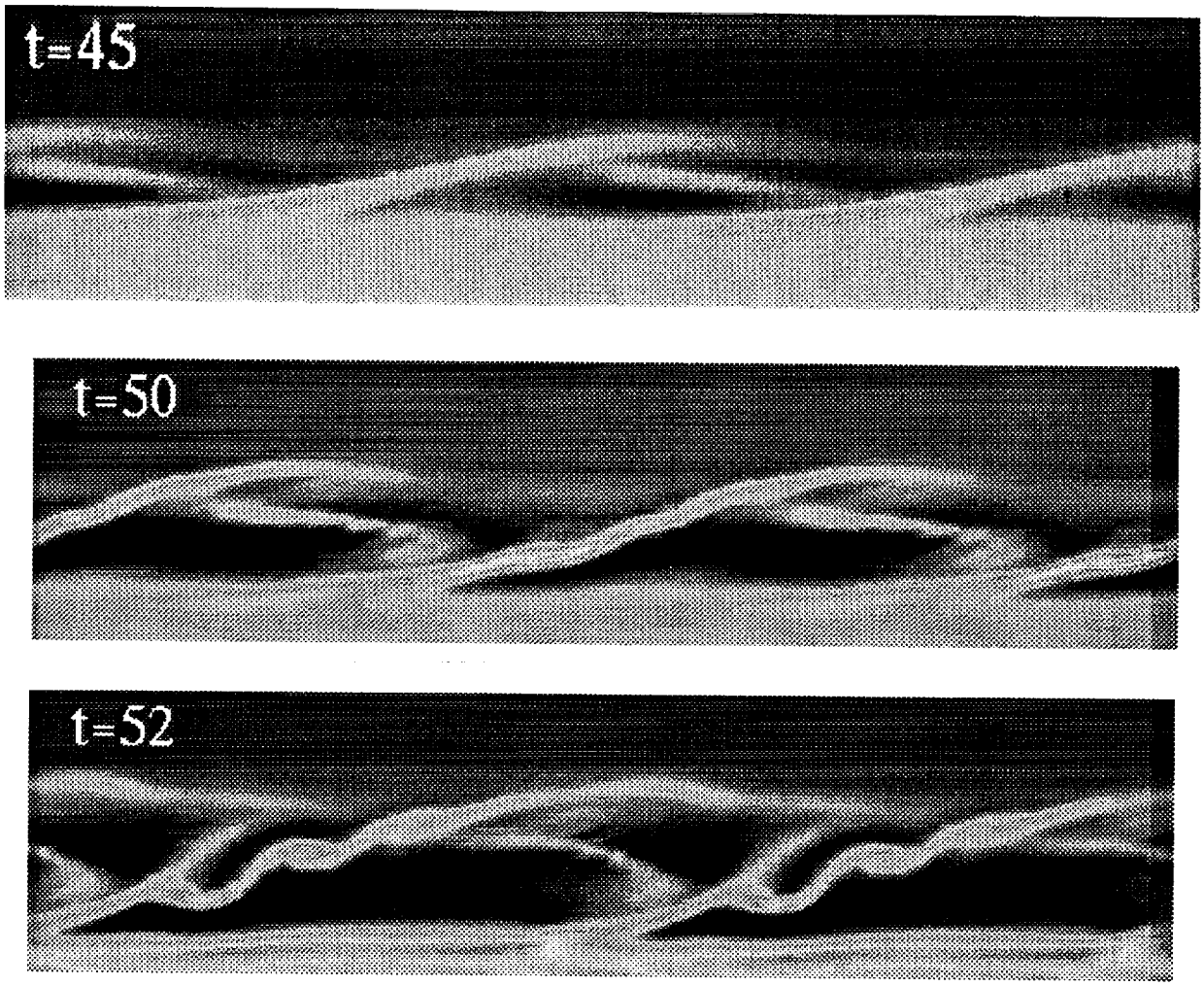

Figure 26. Structure of spanwise vorticity of flow field in transition region with LES and contraction c_1.

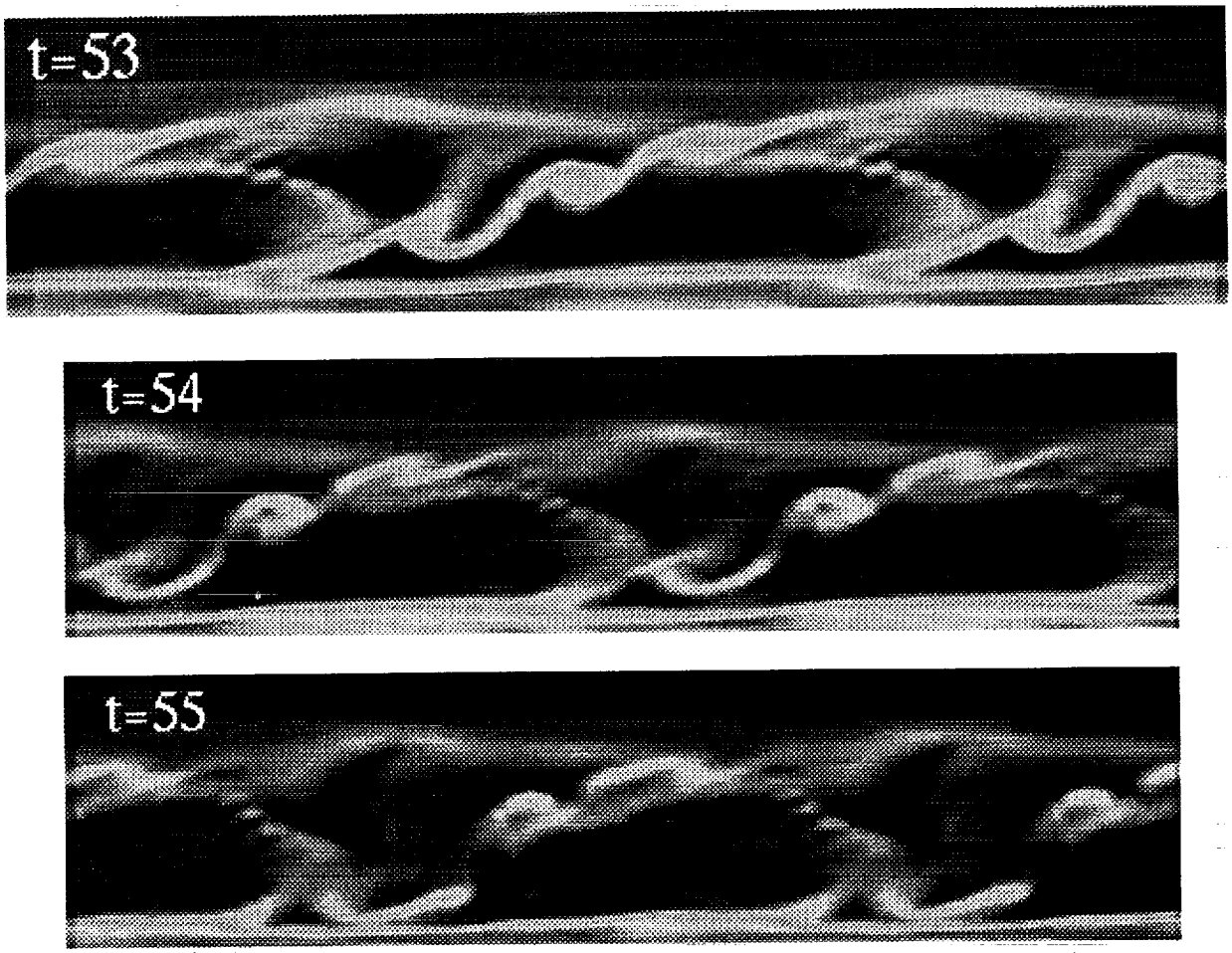

Figure 26. Continued.

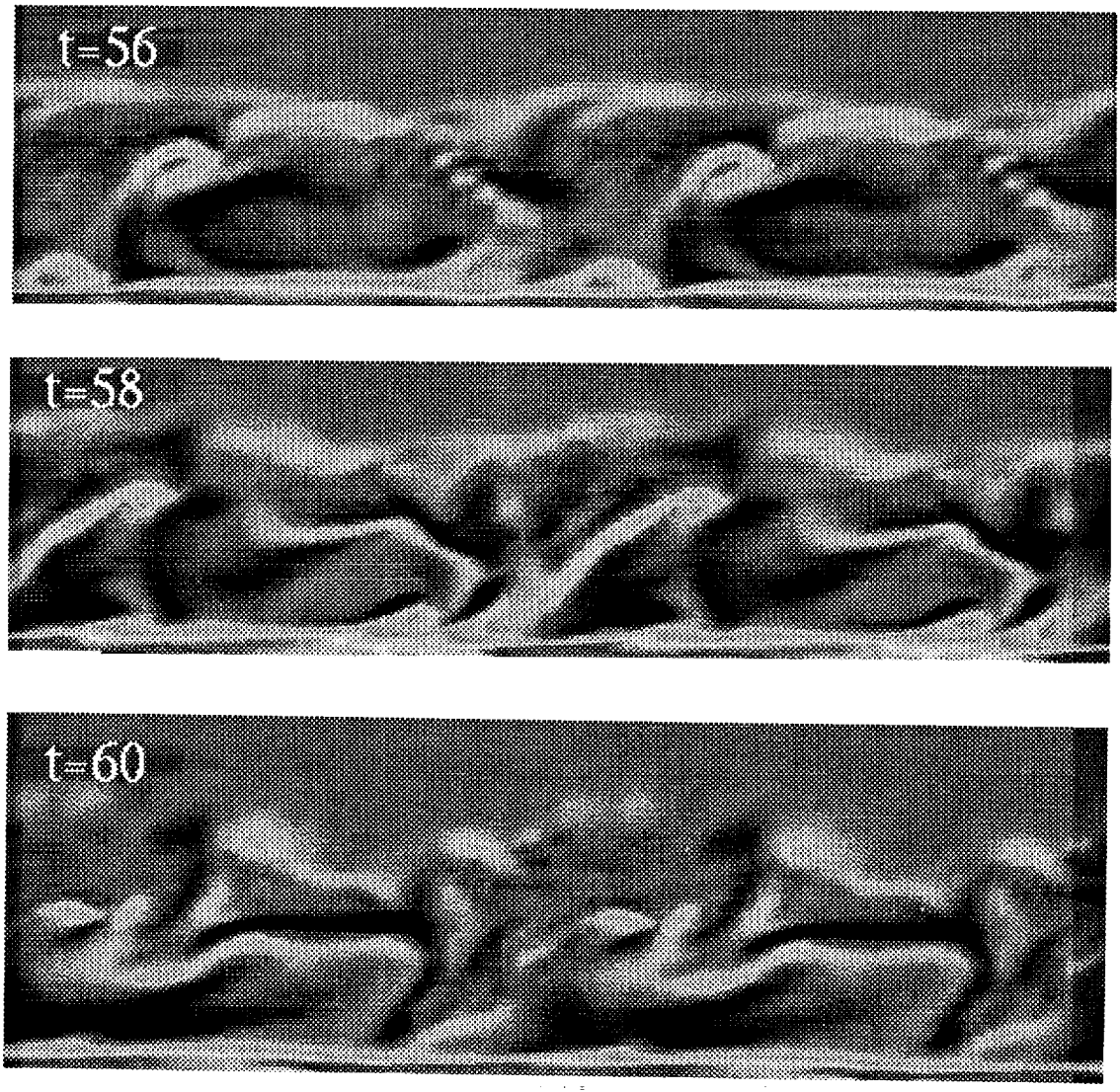

Figure 26. Continued.

REPORT DOCUMENTATION PAGE

Form Approved
OMB No. 0704-0188

1. AGENCY USE ONLY (Leave blank)	2. REPORT DATE	3. REPORT TYPE AND DATES COVERED
	August 1993	Contractor Report

4. TITLE AND SUBTITLE
Large-Eddy Simulation of Laminar-Turbulent Breakdown at High Speeds With Dynamic Subgrid-Scale Modeling

5. FUNDING NUMBERS
C NAS1-19320

WU 505-59-50-01

6. AUTHOR(S)
Nabil M. El-Hady

7. PERFORMING ORGANIZATION NAME(S) AND ADDRESS(ES)
Analytical Services & Materials, Inc.
107 Research Drive
Hampton, VA 23666

8. PERFORMING ORGANIZATION REPORT NUMBER

9. SPONSORING / MONITORING AGENCY NAME(S) AND ADDRESS(ES)
National Aeronautics and Space Administration
Langley Research Center
Hampton, VA 23681-0001

10. SPONSORING / MONITORING AGENCY REPORT NUMBER
NASA CR-4533

11. SUPPLEMENTARY NOTES
Langley Technical Monitor: Craig L. Streett

12a. DISTRIBUTION / AVAILABILITY STATEMENT
Unclassified/Unlimited

Subject Category 34

12b. DISTRIBUTION CODE

13. ABSTRACT (Maximum 200 words)

The laminar-turbulent breakdown of a boundary-layer flow along a hollow cylinder at Mach 4.5 is investigated with large-eddy simulation. The subgrid scales are modeled dynamically, where the model coefficients are determined from the local resolved field. The behavior of the dynamic-model coefficients is investigated through both an a priori test with direct numerical simulation data for the same case and a complete large-eddy simulation. Both formulations proposed by Germano et al. and Lilly are used for the determination of unique coefficients for the dynamic model, and their results are compared and assessed. The behavior and the energy cascade of the subgrid-scale field structure are investigated at various stages of the transition process. The investigations are able to duplicate a high-speed transition phenomenon observed in experiments and explained only recently by the direct numerical simulations of Pruett and Zang, which is the appearance of "rope-like" waves. We also investigate the nonlinear evolution and breakdown of the laminar boundary layer and the structure of the flow field during the transition process.

14. SUBJECT TERMS
large-eddy simulation, laminar-turbulent breakdown, transition modeling, compressible boundary layer, boundary-layer transition

15. NUMBER OF PAGES
60

16. PRICE CODE
A04

17. SECURITY CLASSIFICATION OF REPORT	18. SECURITY CLASSIFICATION OF THIS PAGE	19. SECURITY CLASSIFICATION OF ABSTRACT	20. LIMITATION OF ABSTRACT
Unclassified	Unclassified	Unclassified	